# Sustainable Semiconductor Materials for the Thermoelectric Energy Conversion

by

Xiaoyu Cheng

A thesis

presented to the University of Waterloo

in fulfillment of the

thesis requirement for the degree of

Master of Science

in

Chemistry

Waterloo, Ontario, Canada, 2018

## Author's declaration

I hereby declare that I am the sole author of this thesis. This is a true copy of the thesis, including any required final versions, as accepted by my examiners.

I understand that my thesis may be made electronically available to the public.

## Abstract

Thermoelectric materials can be employed for converting waste energy into feasible electricity through a temperature gradient by utilizing the Seebeck effect (power generation), and vice versa, as coolers by utilizing the Peltier effect.

The most wildly used thermoelectric materials are formed by heavy, often toxic and expensive elements, such as $Bi_2Te_3$ and PbTe. Recent research on magnesium silicide stannide based materials had revealed promising performance with light and abundant elements, and thus the potential to reduce the material cost, making it more favorable for industrial and commercial applications.

The conversion efficiency for thermoelectric material is evaluated by a unitless figure of merit (*ZT*), which is proportional to the power factor value over the thermal conductivity. Doping with Bi and alloying with Sn were proved to be efficient in enhancing the performance of magnesium silicide stannide based material with improved power factors. However, the thermal conductivity is still noticeably high. To further improve the performance, one potential approach is by decreasing the thermal conductivity via alloying with Pb. The presence of Pb introduces additional scattering and mass fluctuations into the solid solution matrix, which should reduce the lattice thermal conductivity significantly. In this study, different amounts of Pb were added into the Bi-doped Mg-Si-Sn solid solutions, and the impact of Pb was investigated.

Due to the failure of the thermal conductivity apparatus, only the electrical properties were experimentally measured, the electronic thermal conductivity was calculated, and conservative estimations were made on the lattice thermal conductivity.

The highest estimated *ZT* of 1.34 was achieved at around 773 K, with the composition of $Mg_2Si_{0.35}Sn_{0.57}Pb_{0.03}Bi_{0.05}$, which is comparable to the highest literature value for the sample without Pb. That being said, with an expected lower lattice thermal conductivity than our estimation, the *ZT* for the sample with Pb is most likely underestimated. All samples revealed similar *ZT* values, and further measurements of the thermal conductivity will be performed to validate the assumption.

**Acknowledgements**

First and foremost, I would like to thank my supervisor, Professor Holger Kleinke, for giving me the opportunity to join this research group, for all his guidance, patience, and his encouraging supervision. I have learnt quite a lot from him throughout my Masters study, he is indeed an awesome chemist, an excellent runner, and also has a really good taste in beer.

I would like to thank my committee members, Professor Pavle Radovanovic, and Professor Eric Prouzet for all their patience and constructive guidance during my Masters research.

I would like to thank Dr. Yu-Chih Tseng from Natural Resources Canada for all his help and advice.

I would like to thank all the help and guidance from, Dr. Jalil Assound, Dr. Leilane Macario, Dr. Simeon Ponou, Dr. Nader Farahi, Dr. Nhi Troung, Yixuan Shi, Parisa Jafarzadeh, Cheryl Sturm, Daniel Ramirez, Luke Menezes, Yonathan Woube, and Mathew VanZant. It was a great pleasure working with you all.

Special thanks to my parents, family, and all my friends, for their love, and support.

I would like to thank Natural Sciences and Engineering Research Council of Canada and the University of Waterloo for the financial support for my research.

## Table of Contents

Author's declaration ..... ii

Abstract ..... iii

Acknowledgements ..... v

List of Figures ..... viii

List of Tables ..... xi

List of Abbreviations ..... xii

1.0 Introduction ..... 1

1.1 Thermoelectric Effects ..... 2

1.2 Conversion Efficiency for Thermoelectric Materials ..... 5

1.3 Approaches to improve thermoelectric performance ..... 7

1.4 Applications of Thermoelectric Materials ..... 9

1.5 State-of-the-Art Materials ..... 11

1.5.1 Materials with Stable Performance at Low Temperatures (300 K – 400 K) ..... 11

1.5.2 Materials with Outstanding Performance at Moderate Temperatures (400 K – 800 K) ..... 12

1.5.3 Materials with Stable Performance at High Temperatures (above 800 K) ..... 14

1.6 Magnesium Silicide Based Thermoelectric Materials ..... 16

1.6.1 Intrinsic defects in $Mg_2E$ (E = Si, Ge, Sn) compounds ..... 20

1.6.2 Enhancing the thermoelectric properties of $Mg_2E$ based materials ..... 21

1.7 Other Group 2 Thermoelectric Silicides ..... 26

1.8 Challenges and Motivations ..... 27

2.0 Experiment Procedures ..... 29

2.1 Synthesis ..... 29

2.1.1 Solid state reaction ..... 29

2.1.1.1 Principle of solid state reactions ..... 29

2.1.1.2 Reaction containers for solid state reaction ..... 31

2.1.1.3 Reaction containers for $Mg_2Si$ based materials ..... 34

2.1.2 Mechanical Alloying ..... 39

2.1.3 Boron oxide flux synthesize method ..... 41

2.2 Characterization ..... 42

2.2.1 Powder X-ray diffraction analysis (P-XRD) ..... 42

2.2.2 Consolidation ..... 44

2.2.3 Density measurement ..... 46

2.2.4 Thermal Diffusivity Measurements ..... 48

2.2.5 Electrical Property Measurements ..... 49

2.2.6 Differential Scanning Calorimetry (DSC) ..... 51

2.2.7 Electron dispersive X-ray spectroscopy (EDX) ..... 52

3.0 Results and discussion ..... 54

3.1 Synthesis ..... 54

3.2 Enhanced performance of magnesium silicide-stannide based material ..... 60

3.3 Sample purity, lattice parameter, and density ..... 62

3.4 SEM and EDX ..... 63

3.5 Physical Property Measurement ..... 69

4.0 Conclusion and future work ..... 82

References ..... 83

## List of Figures

Figure 1. Energy Path for Traditional Combustion Engines.[3] ..... 1

Figure 2. Peltier Effect (left) and Seebeck Effect (right).[5] ..... 4

Figure 3. The Relationship between Different Parameters and Carrier Concentration.[7] ..... 8

Figure 4. Schematic of thermocouples. ..... 9

Figure 5. Cutaway of RTG unit in Galileo.[9] ..... 10

Figure 6. Curiosity rover with thermoelectric power generator.[10] ..... 11

Figure 7. Antifluorite unit cell of $Mg_2E$ (Si, Ge, Sn).[46] ..... 17

Figure 8. Brillouin zone of the $Mg_2E$ lattice.[60] ..... 18

Figure 9. Band structure of $Mg_2Si$.[60] ..... 19

Figure 10. Miscibility gap from $Mg_2Si_{0.4}Sn_{0.6}$ to $Mg_2Si_{0.6}Sn_{0.4}$ (based on [103]). ..... 22

Figure 11. Band structure of $Mg_2Si_{1-x}Sn_x$ solid solutions.[104] ..... 24

Figure 12. Escher painting: fishes to birds.[134] ..... 30

Figure 13. Reaction containers: (a) silica tube, (b) tantalum crucible, (c) sealed tantalum crucible in sealed silica tube, (d) alumina boat. ..... 32

Figure 14. (a) vacuum line, (b) hydrogen-oxygen torch. ..... 33

Figure 15. Arc melting set up. ..... 34

Figure 16. Argon filled glove box. ..... 35

Figure 17. Muffle furnaces: automated (left), manual (right). ..... 36

Figure 18. Niobium foil. ..... 37

Figure 19. (a) graphite foil, (b) customized container. ..... 38

Figure 20. Tube furnace with argon flow. ..... 38

Figure 21. Product after reaction. ..... 39

Figure 22. Fritzsch ball mill machine. ..... 40

Figure 23. Schematic of ball mill motion inside the jar. 41

Figure 24. INEL XRG 3000 powder X-ray diffractometer. 42

Figure 25. Constructive X-ray interference,1 and 2: incident beams, 1′ and 2′: reflected beams 43

Figure 26. (a) Mortar and pestle, (b) grounded product 44

Figure 27. Hot-press instrument. 45

Figure 28. Pressed sample 45

Figure 29. The Sartorius YDK01 density kit. 46

Figure 30. (a) Anter Flashline 3000; (b) Schematic of Flash Method Measurement. 49

Figure 31. ULVAC-RIKO ZEM3. 50

Figure 32. NETZSCH instrument for DSC 51

Figure 33. Quanta FEC 250 EDX machine (left), and working mechanism of EDX (right). 52

Figure 34. Arrangement of reaction containers in the large quartz tube. 54

Figure 35. Heating profile extrapolated from literature. 55

Figure 36. Phase diagram for Mg-Si-Sn system, adopted from [146] 56

Figure 37. Modified heating profile with water quenching. 57

Figure 38. X-ray diffraction analysis for sample with water quenching. 57

Figure 39. Bi-doped $Mg_2Si_{0.4}Sn_{0.6}$ samples with different annealing durations. 58

Figure 40. X-ray diffraction pattern for hot-pressed sample with three days annealing at 973 K.59

Figure 41. X-ray diffraction patterns of $Mg_2Si_{0.35}Sn_{0.6-x}Pb_xBi_{0.05}$ samples, with x = 0, 0.03, 0.05, 0.07, 0.10 62

Figure 42. EDX mapping of $Mg_2Si_{0.365}Sn_{0.6}Bi_{0.05}$ sample, with (a) mapping area; (b) Mg; (c) Si; (d) Sn; (e) Bi represented by different colors. 64

Figure 43. EDX mapping of $Mg_2Si_{0.35}Sn_{0.57}Pb_{0.03}Bi_{0.05}$ sample, with (a) mapping area; (b) Mg; (c) Si; (d) Sn; (e) Bi; (f) Pb represented by different colors. 65

Figure 44. EDX mapping of $Mg_2Si_{0.35}Sn_{0.55}Pb_{0.05}Bi_{0.05}$ sample, with (a) mapping area; (b) Mg; (c) Si; (d) Sn; (e) Bi; (f) Pb represented by different colors..... 66

Figure 45. EDX mapping of $Mg_2Si_{0.35}Sn_{0.53}Pb_{0.07}Bi_{0.05}$ sample, with (a) mapping area; (b) Mg; (c) Si; (d) Sn; (e) Bi; (f) Pb represented by different colors..... 67

Figure 46. EDX mapping of $Mg_2Si_{0.35}Sn_{0.5}Pb_{0.1}Bi_{0.05}$ sample, with (a) mapping area; (b) Mg; (c) Si; (d) Sn; (e) Bi; (f) Pb represented by different colors..... 68

Figure 47. Electrical conductivity of $Mg_2Si_{0.35}Sn_{0.6-x}Pb_xBi_{0.05}$ (x = 0, 0.03, 0.05, 0.07, 0.10), lit. value ($Mg_2Si_{0.365}Sn_{0.6}Bi_{0.05}$) is adopted from [58]. ..... 70

Figure 48. Seebeck coefficient of $Mg_2Si_{0.35}Sn_{0.6-x}Pb_xBi_{0.05}$ (x = 0, 0.03, 0.05, 0.07, 0.10), lit. value ($Mg_2Si_{0.365}Sn_{0.6}Bi_{0.05}$) is adopted from [58]. ..... 71

Figure 49. Calculated energy bands ($\Gamma \rightarrow X$), the convergence area is indicated by red line. From left to right: (a) $Mg_2Si_{0.4}Sn_{0.6}$; (b) $Mg_2Si_{0.4}Sn_{0.54}Pb_{0.06}$; (c) $Mg_2Si_{0.4}Sn_{0.51}Pb_{0.09}$..... 72

Figure 50. Power Factor (*PF*) of $Mg_2Si_{0.35}Sn_{0.6-x}Pb_xBi_{0.05}$ (x = 0, 0.03, 0.05, 0.07, 0.10), lit. value ($Mg_2Si_{0.365}Sn_{0.6}Bi_{0.05}$) is adopted from [58]..... 75

Figure 51. Calculated Lorenz number using SPB model of $Mg_2Si_{0.35}Sn_{0.6-x}Pb_xBi_{0.05}$ (x = 0, 0.03, 0.05, 0.07, 0.10), lit. value ($Mg_2Si_{0.365}Sn_{0.6}Bi_{0.05}$) is adopted from [58]. ..... 76

Figure 52. Electronic thermal conductivity of $Mg_2Si_{0.35}Sn_{0.6-x}Pb_xBi_{0.05}$ (x = 0, 0.03, 0.05, 0.07, 0.10), lit. value ($Mg_2Si_{0.365}Sn_{0.6}Bi_{0.05}$) is adopted from [58]. ..... 77

Figure 53. Lattice thermal conductivity of $Mg_2Si_{0.365}Sn_{0.6}Bi_{0.035}$, adopted from [58]..... 78

Figure 54. Predicted thermal conductivity of $Mg_2Si_{0.35}Sn_{0.6-x}Pb_xBi_{0.05}$ (x = 0, 0.03, 0.05, 0.07, 0.10), lit. value ($Mg_2Si_{0.365}Sn_{0.6}Bi_{0.05}$) is adopted from [58]. ..... 79

Figure 55. Predicted figure of merit of $Mg_2Si_{0.35}Sn_{0.6-x}Pb_xBi_{0.05}$ (x = 0, 0.03, 0.05, 0.07, 0.10), lit. value ($Mg_2Si_{0.365}Sn_{0.6}Bi_{0.05}$) is adopted from [58]. ..... 80

## List of Tables

Table 1. Physical properties of magnesium silicide-stannide based thermoelectric materials ..... 60

Table 2. Lattice parameter refinements on selected samples..... 63

Table 3. Area scan results (percentages) of $Mg_2Si_{0.35}Sn_{0.6}Bi_{0.05}$ sample. ..... 64

Table 4. Area scan results (percentages) of $Mg_2Si_{0.35}Sn_{0.57}Pb_{0.03}Bi_{0.05}$ sample. ..... 65

Table 5. Area scan results (percentages) of $Mg_2Si_{0.35}Sn_{0.55}Pb_{0.05}Bi_{0.05}$ sample. ..... 66

Table 6. Area scan results (percentages) for $Mg_2Si_{0.35}Sn_{0.53}Pb_{0.07}Bi_{0.05}$ sample. ..... 67

Table 7. Area scan results (percentages) for $Mg_2Si_{0.35}Sn_{0.5}Pb_{0.1}Bi_{0.05}$ sample. ..... 68

Table 8. Lattice parameters for electronic structure calculation ..... 73

Table 9. Physical properties of $Mg_2Si_{0.35}Sn_{0.6-x}Pb_xBi_{0.05}$ (x = 0, 0.03, 0.05, 0.07, 0.10), lit. value ($Mg_2Si_{0.365}Sn_{0.6}Bi_{0.05}$) is adopted from [58]. ..... 81

## List of Abbreviations

| | |
|---|---|
| TE | thermoelectric |
| *ZT* | dimensionless figure of merit |
| PGEC | phonon glass electron crystal |
| NASA | the national aeronautics and space ministration |
| RTG | radioisotope thermoelectric generator |
| TAGS | tellurium-antimony-germanium-silver |
| PXRD | powder X-ray diffraction |
| IR | infrared |
| DSC | differential scanning calorimetry |
| SEM | scanning electron microscope |
| EDX | electron dispersive X-ray spectroscopy |
| DFT | density function theory |
| mBJ | modified Becke-Johnson |
| SPB | single parabolic band |
| PF | power factor |
| CBM | conduction band minimum |
| VBM | valence band maximum |

## 1.0 Introduction

Fossil fuel is the main energy source of the world, and based on an estimation, fossil fuel reserves will not be able to support our consumption in around one hundred years, and probably coal will be the only accessible form of fossil fuel after 2042.[1] Moreover, the dependence on the combustion of non-renewable fossil fuels, and the large increases of the global energy consumption, lead to numerous environmental problems; one of them is the greenhouse gas emission. Aside from the negative impact on the environment, the conversion efficiency from fossil fuel to feasible energy is considerably lower than people's expectations; more than half of the energy goes into waste.[2] For example, the traditional internal combustion engine only has an efficiency of 25%. As illustrated by Figure 1, during the working process of a traditional gasoline fueled engine, 40% of the heat from the combustion process is wasted through the exhaust pipe, while another 30% is absorbed by the coolant water. With an additional 5% used for friction and parasitic losses, only 25% of the total energy from burning gasoline is being used to power the vehicle.[3]

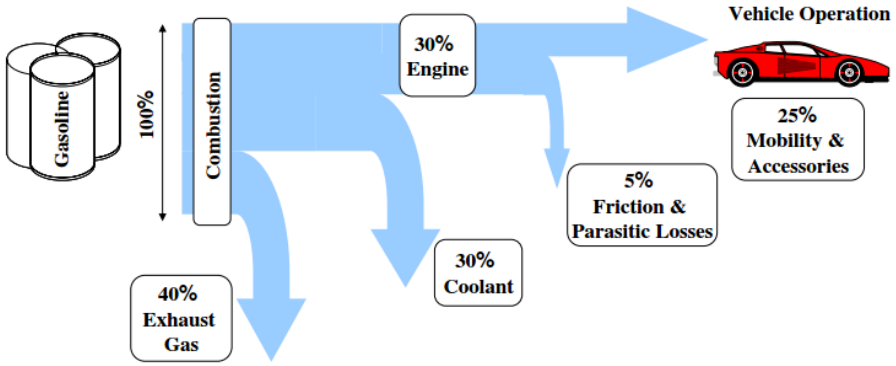


Figure 1. Energy Path for Traditional Combustion Engines.[3]

Numerous approaches have been explored to introduce new energy sources in order to limit the use of fossil fuel and reduce the negative impact of its consumption. Thus, some automobile manufacturers are planning to replace the current combustion engine with an electrical engine. However, the currently available technologies are either very expensive, or takes a long time to implement. Another option consists of harvesting the heat waste, and converting it into usable forms of energy to increase the efficiency, and this is technologically more achievable and easier to apply. Generating useful energy out of waste energy cannot only enhance the efficiency of consuming fossil fuel, but is also beneficial to the environment, since the emission of greenhouse gases can be significantly reduced. To recycle the waste energy, thermoelectric (TE) materials may be employed. Thermoelectric materials are materials that utilize thermoelectric effect, to convert heat into electricity. In this following section, an introduction to thermoelectric effects and thermoelectric materials will be provided.

### 1.1 Thermoelectric Effects

In 1821, a German physicist Thomas Johann Seebeck noticed that when a pair of conductors were connected together, with the two connected junctions placed under different temperature, the charged circuit can deflect a compass needle placed next to it.[4] This interaction was later proved to be a magnetic effect caused by an electric current, which was generated by the temperature gradient between two junctions. A measure of the electric potential generated by unit difference in temperature, is defined by the Seebeck coefficient ($S$), which equals to the value of voltage ($\Delta V$), divided by the difference in temperature ($\Delta T$) (Equation 1).

$$S = \frac{\Delta V}{\Delta T} \qquad \text{Equation 1}$$

Based on Equation 1, the unit of Seebeck coefficient can be written in volts per Kelvin ($V/K$), or as microvolts per Kelvin ($\mu V/K$). The sign of the Seebeck coefficient depends on the type of charge carriers; in *n*-type semiconductors, the Seebeck coefficient is negative, while in *p*-type semiconductors, the Seebeck coefficient is positive.

Thirteen years after the discovery of the Seebeck effect, the French physicist Jean Peltier observed that when an electric current is routed through a pair of conductors, the temperature of both junctions change accordingly.[4] The fluctuation of temperature indicates a heat exchange happened because of the passing current. This phenomenon was considered as a reverse effect of the Seebeck effect, widely known as Peltier effect. However, the principle of the Peltier effect was not illustrated in detail until 1838. Lenz, a physicist, explained that the absorption or generation of heat at the junctions is determined by the direction of the electric current inside the circuit.[4] Similarly, the Peltier coefficient ($\pi$) can be expressed using Equation 2, which is determined by the ratio of the heat generated or absorbed ($Q$) to the electric current running through junction ($I$).

$$\pi = \frac{Q}{I} \qquad \text{Equation 2}$$

The relationship between the Seebeck effect and the Peltier effect was not established until seventeen years later, when William Thomson built the theoretical connection between the two thermoelectric effects, giving rise to the Thomson effect.[4] The Thomson effect describes the heat exchange happening when passing a current through a conductor under a temperature gradient. If the carriers are moving along the gradient, heat will be released, otherwise heat will

be absorbed. In the Thomson effect, the Peltier coefficient ($\pi$) is related to the Seebeck coefficient ($S$), and the connection can be illustrated in Equation 3.

$$\pi = S \cdot T \qquad \text{Equation 3}$$

These phenomena can be explained by the movement of charge carriers within the paired generator with respect to temperature difference and thermal excitation. There are two different types of charge carriers: electrons are carriers having negative charge, and holes are carriers having positive charge. In thermoelectric devices, the thermoelectric materials mainly utilize the Seebeck effect and the Peltier effect, and the principles of them are illustrated in Figure 2.[5]

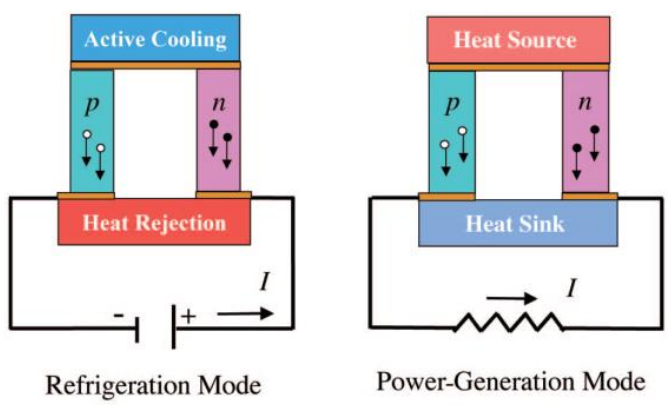


Figure 2. Peltier Effect (left) and Seebeck Effect (right).[5]

## 1.2 Conversion Efficiency for Thermoelectric Materials

By evaluating the conversion efficiency, the unit less figure-of-merit was introduced by Abram Fedorovich Ioffe in 1957.[6] After derivation, the figure-of-merit can be expressed as in Equation 4.

$$ZT = \frac{S^2\sigma}{\kappa}T \qquad \text{Equation 4}$$

In Equation 4, $S$ represents the Seebeck coefficient, $\sigma$ represents the electrical conductivity, $\kappa$ represents the thermal conductivity, and $T$ indicates the absolute temperature. The temperature used in calculation of $ZT$ is the average temperature across the material. The efficiency of a thermoelectric generator can be calculated via Equation 5. Where $\eta$ is efficiency, while $T_H$ and $T_C$ are the temperatures of the high temperature end and low temperature end, respectively, with $ZT$ standing for the figure-of-merit.

$$\eta = \frac{T_H - T_C}{T_H} \cdot \frac{\sqrt{1+ZT} - 1}{\sqrt{1+ZT} + \frac{T_C}{T_H}} \qquad \text{Equation 5}$$

To obtain a higher efficiency, a higher $ZT$ value is advantageous. According to Equation 4, the $ZT$ value is proportional to $S^2\sigma$, and has an inverse relationship with $\kappa$. The strategy to improve the performance seems to be straightforward: maximizing the value of $S^2\sigma$, while controlling the thermal conductivity at a relatively low level. However, the interrelationship between different parameters makes the optimization of conditions much more difficult.

The Seebeck coefficient can be calculated via Fermi-Dirac statistics in case of degenerate semiconductors or metals:

$$S = \frac{8\pi^2 {k_B}^2}{3eh^2} m^* T \left(\frac{\pi}{3n}\right)^{2/3}. \qquad \text{Equation 6}$$

Where $k_B$ is the Boltzmann constant, $e$ is the carrier charge, $h$ indicates the Planck's constant, $m^*$ is the effective mass of the charge carrier, and $n$ is the carrier concentration. In Equation 6, there is roughly an inverse relationship between the carrier concentration and the value of the Seebeck coefficient.

The electrical conductivity can be described by Equation 7:

$$\sigma = \frac{1}{\rho} = n\mu e \ . \qquad \text{Equation 7}$$

Where $r$ represents the resistivity, $e$ is the carrier charge, $n$ is the carrier concentration, and μ is the carrier mobility. According to Equation 7, electrical conductivity increases with an increasing charge carrier concentration.

The third determining factor of $ZT$ is the value of thermal conductivity, $\kappa$. As shown in Equation 8, $\kappa$ consists of two parts: the contribution from the lattice, $\kappa_l$, and the contribution from the electronic aspect, $\kappa_e$. $\kappa_e$ is proportional to the electrical conductivity as shown in Equation 9:

$$\kappa_{tot} = \kappa_e + \kappa_l \qquad \text{Equation 8}$$

$$\kappa_e = L\sigma T \qquad \text{Equation 9}$$

The impact of $\kappa_e$ on $\kappa_{tot}$ is often smaller than $\kappa_l$. $\kappa_l$ can be represented by the following equation:

$$\kappa_l = \frac{1}{3}\left(C_v V_s \lambda_{ph}\right) \qquad \text{Equation 10}$$

Where $C_v$ is the heat capacity, $V_s$ is the velocity of sound, and $\lambda_{ph}$ is the phonon mean free path.

### 1.3 Approaches to improve thermoelectric performance

There is no theoretical ceiling on the value of *ZT*, but the recent research reveals that a *ZT* value greater than 1 is desired to exhibit efficient thermoelectric properties, and for power generation, a *ZT* greater than 1.5 is preferred, for cooling, the material needs to retain a *ZT* value around 2 to 4.[7] Efforts are made to improve the efficiency, different approaches were performed, and doping is one of the most efficient method. During doping, a lattice atom is substituted by a dopant, while the crystal structure remains the same. The presence of dopant has a huge impact on carrier concentration and mobility. The dopant usually starts with a trace amount, and increases stepwise. The relationship between carrier concentration and the values of different parameters is illustrated in Figure 3.[7]

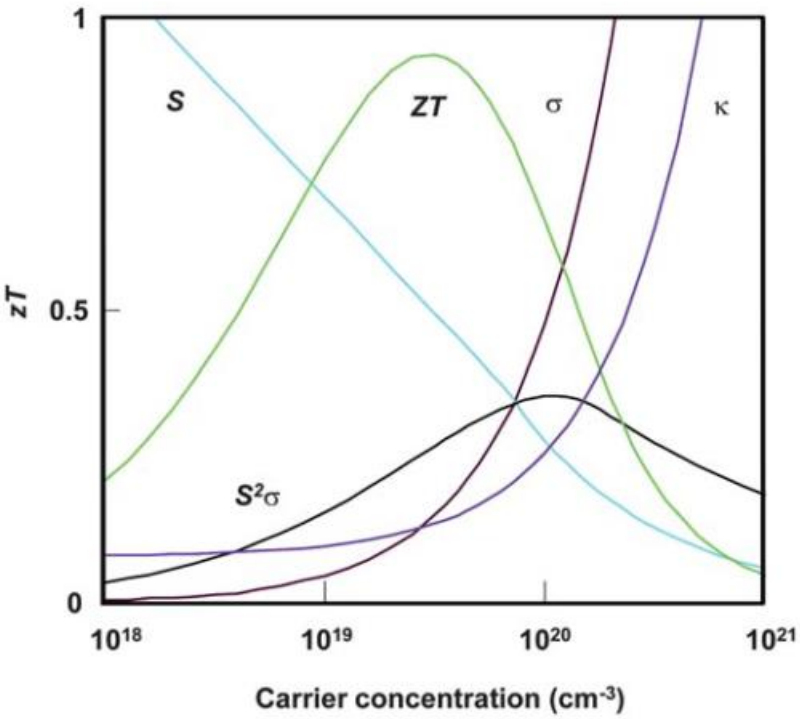


Figure 3. The Relationship between Different Parameters and Carrier Concentration.[7*]

Material with the best thermoelectric properties are mostly semiconductors with high carrier concentration and low $\kappa_l$. The three key parameters cannot be evaluated separately, as for instance the electrical conductivity increases together with the thermal conductivity with an increasing carrier concentration, and the Seebeck coefficient decreases along with the increasing carrier concentration. In order to enhance the performance, one needs to find the balance between the values of the determining parameters. An ideal type of material is called the PGEC material, which stands for a phonon glass and an electron crystal.[4] PGEC describes the specific property of a material in which the phonon mean free path can be as short as in a glass, and in

[*] Reprinted by permission from Macmillian Publishers Ltd: [Natural Materials] (Snyder, G. J.; Toberer, E. S. Complex Thermoelectric Materials. Nat. Mater. 2008, 7, 105–114.), copyright (2008)

which the electron mean free path can be as long as in a crystal; with such a material, the balance between different parameters can be achieved, hence the performance of thermoelectric material is enhanced.

### 1.4 Applications of Thermoelectric Materials

One of the widely used applications of thermoelectric materials is the thermocouple, which is used to determine the temperature by utilizing the Seebeck effect. Two different types of alloys (or metals) are used to form a circuit with one junction connected, where the temperature is tested, and the other junction attached to a voltmeter, which indirectly gives the measurement of temperature, when the Seebeck coefficient is known. A schematic of thermocouples is shown in Figure 4.[8] The temperature difference between the two junctions can be reflected as current passing through the circuit, and then the temperature of the tested end can be determined based on the relationship between temperature and voltage.

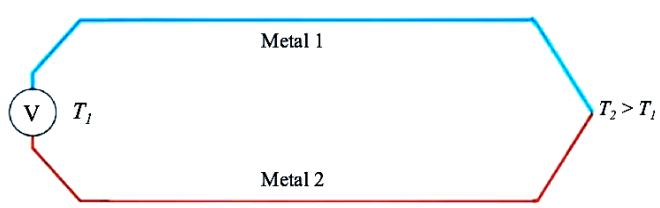


Figure 4. Schematic of thermocouples.

Another potential application of thermoelectric materials is harvesting the waste energy during the working process of traditional combustion engine powered vehicle. The conversion efficiency of a combustion engine is as low as 25%, as a huge amount of energy goes into waste

heat during the working process, and the exhaust gas can be heated up to 500 ºC.[3] The huge difference in temperature between exhaust gas and cooling system can thus be utilized via the Seebeck effect, converting the temperature gradient into electricity, and supplying other parts with electricity like heated seats and air conditioning systems.

Thermoelectric materials can also be used in deep space exploration programs. NASA applied the Radioisotope Thermoelectric Generators (RTG) in converting the heat of the radioactive decay process of plutonium-238 into usable electricity. These thermoelectric generators were proved to be efficient and reliable enough for this application, and were thus applied in multiple missions lead by NASA, such as the Galileo (Figure 5),[9] and the curiosity mars rover (Figure 6).[10]

Thermoelectric materials can also be used in cooling systems. IBM recently developed thermoelectric material based cooler modules for memory and chips, which are based on Peltier effect.[11] Moreover, thermoelectric materials are also used in refrigeration products like refrigerators.

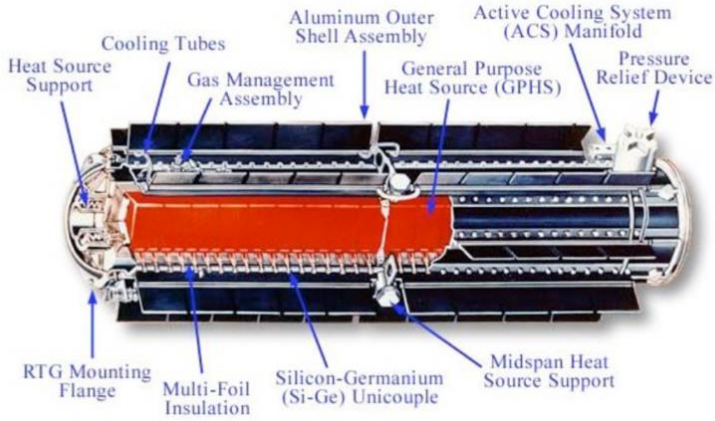


Figure 5. Cutaway of RTG unit in Galileo.[9]

Figure 6. Curiosity rover with thermoelectric power generator.[10]

### 1.5 State-of-the-Art Materials

Numerous materials have been considered and studied as potential candidates for thermoelectric applications. In this section, thermoelectric materials with promising performance are discussed and categorized by their working temperature.

#### 1.5.1 Materials with Stable Performance at Low Temperatures (300 K – 400 K)

When the working temperature remains at relatively low level, materials based on $Bi_2Te_3$ are preferred. Results from Habman's research in 1957[12] show that the energy gap of $Bi_2Te_3$ is 0.16 eV at 300 K, while the carrier concentration is $8\times10^{18}$ $cm^{-3}$ for holes, and $5\times10^{18}$ $cm^{-3}$ for electrons. For $Sb_2Te_3$, the energy gap is around 0.28 eV, with a carrier concentration level

around $10^{20}$ $cm^{-3}$,[4] and for $Bi_2Se_3$, the energy gap is around 0.08 eV, with a carrier concentration level around $10^{19}$ $cm^{-3}$.[13] Both the *n*-type $Bi_2Te_3$ and the *p*-type $Sb_2Te_3$ have high *ZT* values about 1 at around 300 K.[14] Apart from the bulk material, the $Bi_2Te_3$ base solid solutions $Bi_2(Te_xSe_{1-x})_3$ and $(Bi_{1-x}Sb_x)_2Te_3$ also revealed good thermoelectric properties. The p-type $Bi_{0.3}Sb_{1.7}Te_3$ achieved a high *ZT* of 1.3.[15] The nano-structured $Bi_{0.48}Sb_{1.52}Te_3$ solid solution achieved a high *ZT* of 1.4 at around 300 K.[16] Nano-structuring is considered as one of the most effective method to improve the performance of thermoelectric material. Nano-structuring is typically achieved by adding nano-composites to create additional interfaces, which will in turn scatter the mid wavelength and long wavelength phonons, thus reducing the lattice thermal conductivity, and enhancing the *ZT* value.[17] Recent research on the large scale synthesis of the p-type $Bi_2(Sb, Te)_3$ was conducted, with 3 to 5 kilograms of product being synthesized, and a high *ZT* above 1 was achieved around 350 K.[18]

### 1.5.2 Materials with Outstanding Performance at Moderate Temperatures (400 K – 800 K)

The $Bi_2(Se, Te)_3$ based compound also has promising performance at moderate temperatures;$Bi_{0.4}Sb_{1.6}Te_3$ with 0.2 vol% CuO added by nanoinclusion achieved a high *ZT* of 1.37 at 496 K.[19]

With a carrier concentration level around $1.6\times10^{19}$ $cm^{-3}$,[20] the silver antimony telluride $AgSbTe_2$ based material has been considered as one option with a band gap of 0.35 eV.[21] Doping was proved to be efficient in enhancing the performance; the thermal conductivity was reduced significantly with Se doping, with a *ZT* value of 1.4 around 560 K.[20]

The lead antimony silver telluride based materials are also thermoelectric materials with promising performance at moderate temperatures. These materials have the formula of

$Ag_nPb_mM_nTe_{m+2n}$, where M can be either antimony or bismuth. The structure can be considered as a rock salt structure, where the Na sites of rock salt structure are occupied by silver, lead, and M; the Cl sites are occupied by tellurium atoms. One of the compositions, with a formulation of $AgPb_{10}SbTe_{12}$ has a relatively stable performance with high Seebeck coefficient. When n = 1, and m = 18, the material's maximal ZT value is around 2.1 at a temperature of 800 K.[22] The lead antimony sliver telluride material (LAST) can also be modified. Lead atoms in LAST system are partially replaced by tin atoms, generating lead-antimony-silver-tellurium-tin compounds, which can also be written as LASTT. The LASTT material's maximal ZT value is around 1.5 at a temperature of 627 K.[23]

Cobalt triantimonide ($CoSb_3$), a member of the family of skutterudite, adopts the $CoAs_3$ structure, and has a band gap of 0.57 eV,[24] with a carrier concentration of $4\times10^{17}$ $cm^{-3}$.[25] Cobalt triantimonide itself has a solid performance with *ZT* value around 0.8 at 600 K.[14] On the basis of cobalt triantimonide, the skutterudites with filled structure possess excellent performance. The compounds with this modified structure can be formulated as $RE_xM_4Q_{12}$, while RE can be lanthanide elements, such as lanthanum (La), cerium (Ce), or praseodymium (Pr), while M can be iron (Fe), ruthenium (Ru), or osmium (Os), and Q can be phosphorus (P), arsenic (As), or antimony (Sb).[26] According to research conducted recently, the Fe-based modified skutterudite has a *ZT* value of 1.4 at 873 K, with the formula of $CeFe_{4-x}Co_xSb_{12}$.[27] The Yb filled skutterudite has a *ZT* value of 1.0 at 600 K.[28] The Ba and Yb filled cobalt triantimonide based materials also have high *ZT* values of 1.4 at 800 K.[29]

The ternary thallium tellurides ($Tl_{10-x}E_xTe_6$) based material also revealed excellent thermoelectric properties (E can be different elements, including lanthanides, Sn, Pb, Sb, and Bi). The compound with Bi achieved a high *ZT* of 1.2 at around 500 K after zone-melting, and a

high *ZT* of 0.9 at around 500 K for the compound with Sb.[30] The sample with the composition of $Tl_{8.95}Sn_{1.95}Te_6$ displayed a high *ZT* of 1.26, and $Tl_{8.10}Pb_{1.90}Te_6$ revealed the highest *ZT* of 1.46 in this family, both around 685 K.[31] For the thallium lanthanide tellurides, a *ZT* value of 0.57 was achieved with $Tl_9LaTe_6$ at around 600 K.[32]

### 1.5.3 Materials with Stable Performance at High Temperatures (above 800 K)

For radioisotope thermoelectric generators used by NASA in their space missions, one requirement is to withstand extreme working conditions like high temperature. Thus, silicon-germaniums solid solutions appeared to fulfill the requirement. $Si_{1-x}Ge_x$ material can deliver a sufficient performance from 600 K to 1300 K, and according to literature, as a *n*-type material, $Si_{0.8}Ge_{0.2}$ can reach a *ZT* value of 1.0 at around 900 K.[33] Both Si and Ge maintain the diamond structure, and their lattice parameters are comparable: 5.43 Å for Si and 5.66 Å for Ge. The similarity in their structures has its benefits: the Si-Ge solid solution can be formed with a wide range of compositions.

Lead telluride based materials and lead-tin tellurides (PbTe and $Sn_xPb_{1-x}Te$) are considered potential candidate for thermoelectric materials under a working temperature range from 500 K to 900 K.[34] The intrinsic PbTe has a range of carrier concentrations between $2 \times 10^{18}$ $cm^{-3}$ to $1.7 \times 10^{19}$ $cm^{-3}$, and an energy gap of 0.32 eV at room temperature. Following the Vegard's law, the Sn-Pb telluride system forms a solid solution within a certain range, and the energy gap varies according to the carrier concentrations that are determined by the composition. For most of the *n*-type doping, $PbI_2$ and $PbBr_2$ are usually employed, and for *p*-type doping, $Na_2Te$ and $K_2Te$ are usually added. The PbTe based thermoelectric material was applied as RTG devices in NASA's space missions.[35] A *ZT* of 1.4 was discovered for $PbTe_{1-x}I_x$ under a

temperature range from 700 K to 850 K,[36] and a *ZT* of 1.4 for $Na_xPb_{1-x}Te$ at the same temperature range.[37] PbSe (lead selenide) was also considered as a promising thermoelectric material, with a similar electronic structure to PbTe; the material revealed a high *ZT* of 1.2 at 850 K.[38] Recently, a solid solution with the composition of $PbSe_{0.2}Te_{0.8}$ doped with 8% MgTe was revealed to exhibit a high figure of merit of 2.2 at around 800 K.[39]

Despite the fact that PbTe based materials exhibit superb performance, people still are concerned about lead's toxicity. Thus, the Tellurium-Antimony-Germanium-Silver (TAGS) based materials were studied as less toxic alternatives to PbTe - noting that tellurium is toxic as well, but to a smaller degree. The TAGS material has low thermal conductivity from 300 K to 900 K. The TAGS material was fabricated using $AgSbTe_2$ with GeTe, and with the presence of 75% to 90% GeTe, the TAGS material will undergo a structural transition from rhombohedral to cubic at room temperature.[40] The minimum lattice thermal conductivity was achieved with the material that has 80% GeTe and 85% GeTe (TAGS-80 and TAGS-85), which is less than 0.8 W $m^{-1}K^{-1}$.[41] A high *ZT* of 1.8 was also achieved with TAGS-80 at around 773 K,[41] and a high *ZT* of 1.5 with TAGS-85 based material at 730 K.[42] The large scale production of the TAGS material was also reported, with a high *ZT* of 1.56 obtained for TAGS-90 (with 90% GeTe), and 1.48 for TAGS 80 at around 650 K.[43]

The half-Heusler compounds are also materials that can operate at high temperature. Half-Heusler compounds can be formulated as XYZ, in which X represents early transition metals, essentially Ti, Zr, or Hf; Y can be mid-transition metals Co or Ni, and Z can be *p*-block elements like Sn or Sb. In half-Heusler, the Z element forms the face-centered cubic lattice, with the X element filling all octahedral sites, and the Y element occupying half of the tetrahedral sites. With doping, the performance of the half-Heusler material was improved, and the Half-

Heusler compound with a formula of $Ti_{0.5}(Zr_{0.5}Hf)_{0.5}NiSn_{0.998}Sb_{0.002}$ reached a *ZT* value of 1.5 at around 700 K.[44] The compound with a formula of $Zr_{0.5}Hf_{0.5}CoSb_{0.8}Sn_{0.2}$ was reported to possess an *ZT* value of 0.8 at 973 K.[45]

### 1.6 Magnesium Silicide Based Thermoelectric Materials

Magnesium is an alkaline earth metal with two valence electrons. Magnesium can form compounds $Mg_2E$, where E represents elements of group 14, namely carbon, silicon, germanium, tin, and lead. $Mg_2E$ adopts an antifluorite structure. In the unit cell of $Mg_2EE$ forms a face centered cubic packing, with Mg atoms occupying all eight tetrahedral holes.[46] The unit cell of $Mg_2E$ is illustrated in Figure 7, with the blue spheres representing E , and the red spheres Mg atoms. However, not all $Mg_2E$ materials are useful thermoelectrics. $Mg_2C$ is not stable unless under high pressure,[47] and $Mg_2Pb$ can be considered as a semimetal, with a band gap of -0.15 eV.[46,48] Therefore, when discussing thermoelectrics, only $Mg_2Si$, $Mg_2Ge$, and $Mg_2Sn$ are considered. Those $Mg_2E$ (E = Si, Ge, Sn) materials and their solid solutions exhibit semiconducting character, which qualify them as promising candidates for thermoelectric materials.

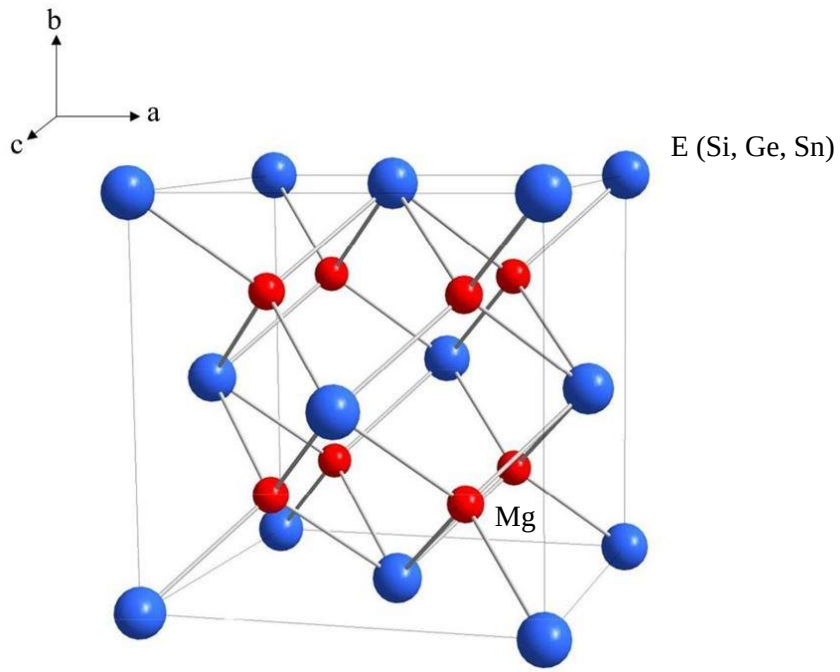


Figure 7. Antifluorite unit cell of $Mg_2E$ (Si, Ge, Sn).[46]

Various synthesis methods were considered in literature, such as vertical gradient freezing method,[49] microwave synthesis,[49] combustion reaction,[52] vertical Bridgman method,[53] synthesis using existing salts such as NaSi and $MgCl_2$,[54] $B_2O_3$ flux method,[55] mechanical alloying,[56,57] enclosed solid state reaction combined with mechanical alloying.[58]

The chemical bonding in $Mg_2Si$ was determined to be mostly covalent, with an estimated ionicity around 10%.[59] As a guide to understand the band structure plot, the Brillouin zone of the $Mg_2E$ lattice is shown in Figure 8. The plotted band structure corresponds to the following high symmetry directions of the Brillouin zone: $L \rightarrow \Gamma \rightarrow X \rightarrow W \rightarrow K \rightarrow \Gamma$. To interpret the band structure, it can be viewed as derived from the interactions between valence orbitals of Mg atoms and E atoms. The resulting bands are filled up with the contributing valence electrons from the *s* orbital of Mg the *s* and *p* orbitals of E.[60] The calculated energy gap was determined to be 1.3 eV

for $Mg_2Si$, slightly higher compared to the experiment value of 0.77 eV.[61] The band gap for $Mg_2Ge$ was calculated to be 0.74 eV,[60] and the band gap for $Mg_2Sn$ was determined to be 0.35 eV.[61]

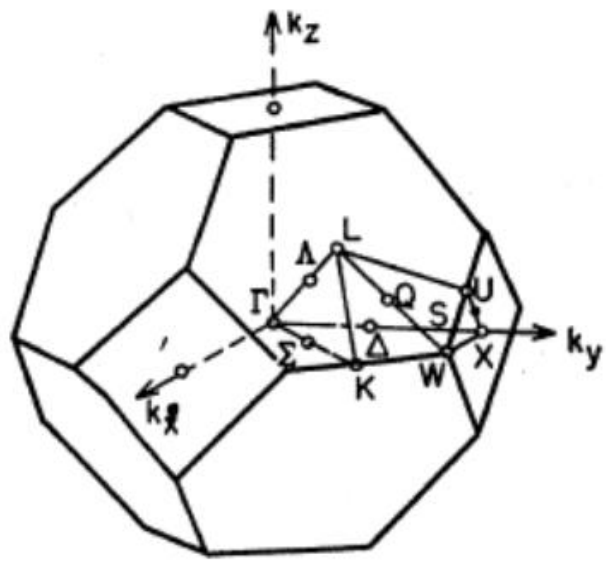


Figure 8. Brillouin zone of the $Mg_2E$ lattice.[60†]

† Reprinted (figure) with permission from (P.M. Lee, Review, *135*, A1110, **1964**) Copyright (1964) by the American Physical Society http://dx.doi.org/10.1103/PhysRev.135.A1110.

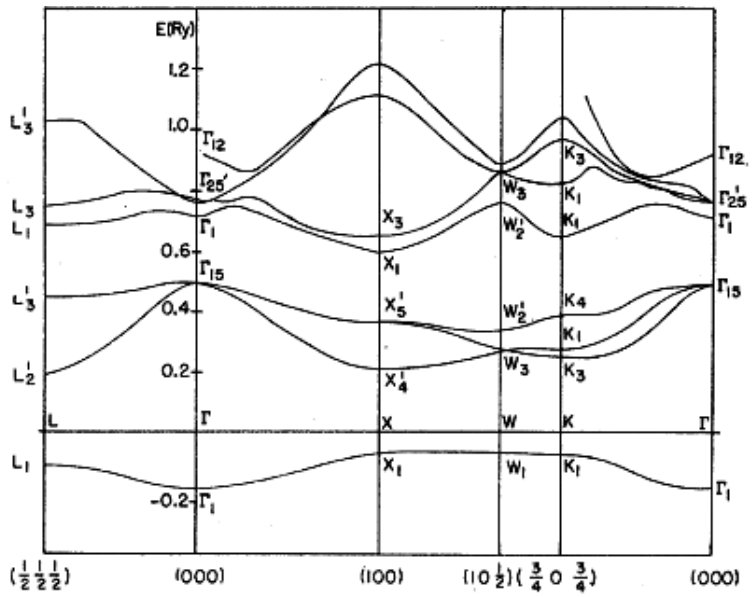


Figure 9. Band structure of $Mg_2Si$.[60‡]

Materials properties are primarily determined by the character of bonding. Because Si has a similar (Pauling) electronegativity (1.90) compared to Ge (2.01) and Sn (1.96), the covalent character of the bonding is expected to be similar as well.

All the $Mg_2E$ compounds consist of the same structure, and their lattice parameters vary with different E atomic radius, with $a$ = 6.351 Å for $Mg_2Si$,[62] 6.385 Å for $Mg_2Ge$,[63] 6.765 Å for $Mg_2Sn$,[64] and 6.815 Å for $Mg_2Pb$.[65] The melting points also differ for the different compounds, with 1375 K for $Mg_2Si$, 1388 K for $Mg_2Ge$, 1051 K for $Mg_2Sn$, and 823 K for $Mg_2Pb$, respectively.[48]

‡ ‡ Reprinted (figure) with permission from (P.M. Lee, Review, *135*, A1110, **1964**) Copyright (1964) by the American Physical Society http://dx.doi.org/10.1103/PhysRev.135.A1110.

### 1.6.1 Intrinsic defects in $Mg_2E$ (E = Si, Ge, Sn) compounds

A perfect crystal with all the atoms sitting on their own sites is a philosophical ideal that only exists at zero Kelvin. Above $T$ = 0 K, defects arise from entropic effects, which include thermal vibration at elevated temperature, the misplacement of atoms, and even the addition (interstitial) or vacancy (point defect) of atoms. When the disorders occur without modification of the composition, there are only stoichiometric defects present in $Mg_2E$ (E = Si, Ge, Sn) crystal. With more magnesium than desired stoichiometry, the additional Mg atoms sit on empty octahedral sites and create interstitial Mg defects ($Mg_I$).[66] On the contrary, reduction on stoichiometry amount create Si vacancies ($V_{Si}$).[66] Another possible defect in $Mg_2E$ is the anti-site defect, which was created by the misplacement of Mg atoms on Si sites ($Mg_{Si}$).[66]

Without any dopant, intrinsic $Mg_2Si$ revealed *n*-type character. According to results from first principle studies, because of the low formation energy required, the preferred defect under stoichiometric conditions during synthesis is Mg atoms on interstitial sites ($Mg_I$), and the negative charge carriers (electrons) are donated by $Mg_I$.[67] Under Mg-rich condition, $Mg_I$ type defects are also preferred.[67] Even with insufficient amount of Mg, since it requires relatively low formation energy compare to other types of defects, $Mg_I$ type defect is still observed. On the contrary to $Mg_2Si$, $V_{Mg}$ is the preferred defect type in stoichiometrically synthesized $Mg_2Ge$, which was mainly because of the loss of Mg under high temperature solid state synthesis.[68] The $V_{Mg}$ donates *p*-type carriers, and contributes to *p*-type properties. The Mg content in the lattice can be altered by an increased amount during the synthesis, and with the excess amount of Mg being added, the interstitial Mg becomes the majority of defects, and the material can be transferred from $V_{Mg}$ dominated *p*-type to $Mg_I$ dominated *n*-type.[68] In $Mg_2Sn$, $V_{Mg}$ was revealed to be the major defect regardless the excess or insufficient amount of Mg, thus the intrinsic

$Mg_2Sn$ exhibits *p*-type properties. The $V_{Mg}$ is more favorable compare to $Mg_I$ and $Sn_{Mg}$, which is mainly because of the difference in atomic radius between Mg and Sn atoms. Thus, $Mg_2Sn$ has a larger interstitial space compare to $Mg_2Si$, which leads to unstable formation of $Mg_I$ type defects.[69]

### 1.6.2 Enhancing the thermoelectric properties of $Mg_2E$ based materials

The bulk $Mg_2Si$ material has a relatively low electrical conductivity as well as a large band gap. To improve its thermoelectric performance, different approaches were carried out, with doping and solid solutions formation being the most efficient methods. In doping, the band gap can be reduced, and carriers added, leading to enhanced performance. Doping can be achieved by introducing hetero-atoms into intrinsic semiconductors. The dopants can donate or combine the charge carriers, thus altering the carrier concentration. The doped semiconductors can be classified based on the nature of their charge carriers: the material with negative carriers is called *n*-type semiconductor, and the material with positive carriers is called *p*-type semiconductor. Since doping has a dramatic effect on carrier concentration and carrier mobility, it is suggested to start with a small doping level. Different dopants may apply in order to tune the structure transport properties. For *n*-type doping, some work was dedicated with group 3 elements, such as scandium, yttrium, and lanthanum.[70,71] But other elements were also used, for instance cobalt, copper, and zinc.[72–74] Elements from group 13 to 17 were adopted as dopants as well, including boron, aluminum, phosphorus, antimony, bismuth, selenium, and tellurium.[58,75–84] For *p*-type doping, elements from group 1 were employed as the major candidates, including lithium, sodium, and potassium.[85–88] Apart from group 1 elements, silver and gallium were also reported as *p*-type dopants.[88–91] Group 14 elements were used as components for solid solutions,

the band structure was tuned dramatically, and the thermoelectric performance was improved effectively with the presence of germanium, tin, and lead.[58,92–99]

Among all the advantages that $Mg_2Si$ based material has, a particularly important one is the ability in forming an incredibly wide range of solid solutions with germanium and tin, even with lead, because all the $Mg_2E$ (E = Si, Ge, Sn, Pb) based materials are isostructural, adopting the anti-fluorite type structure. Germanium can form solid solutions with $Mg_2Si$ on the entire range, with a composition of $Mg_2Si_xGe_{1-x}$ ($0 \leq x \leq 1$). In the case of tin, with a similar composition of $Mg_2Si_xSn_{1-x}$, there is a miscibility gap reported with x ranging from 0.4 to 0.6.[100] However, some suggested that the miscibility can be overcame with proper synthesis method, and the desired compositions that are located within the originally reported miscibility gap can be stabilized.[55,101]

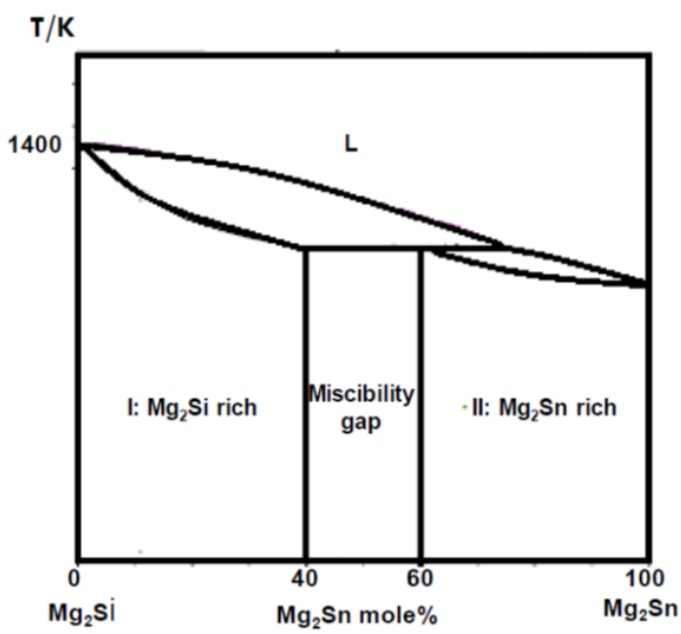


Figure 10. Miscibility gap from $Mg_2Si_{0.4}Sn_{0.6}$ to $Mg_2Si_{0.6}Sn_{0.4}$ (based on [102]).

Forming solid solutions with heavier elements, the formula weight of $Mg_2Si$ based material is increased, and the thermal conductivity is significantly lowered. In this case, the substitution atom can be viewed as "impurity", which acts differently from the original atom with a different size, a different mass, and different bond strength. Those differences create disorder in the lattice, and the phonon scattering process is significantly enhanced, which in turn lower the lattice thermal conductivity.

Besides the intensive phonon scattering created by substituting silicon (Si) with germanium (Ge) and tin (Sn), the band structure is also greatly modified by the substitutions. The presence of multiple conduction band minima (referred as band convergence) is an indication of possibly high performance materials, and can be induced by point defects. An example with first principle calculations on $Mg_2Si_{1-x}Sn_x$ solid solutions, with x varying from 0 to 1 is illustrated in Figure 11.[103] The general trend of the highest valence band and two lowest conduction band was shown in the figure, with the blue line indicates the light conduction band ($C_L$), and the red line indicates the heavy conduction band ($C_H$). There is an energy separation of $\Delta E$ between the two lowest conduction band as well. From the range with x = 0 to x = 1, the heavy conduction band moves downwards in energy, with the light conduction band moves downwards before x = 0.3, and moves upwards after x = 0.3. The two conduction bands cross around a composition where x = 0.65 to 0.7. In a semiconductor with two conduction bands, the total Seebeck coefficient can be considered as the weighted average stemming from both conduction bands, and the maximum value can be achieved when the two conduction bands have equal contributions towards the total Seebeck coefficient, and the maximum effective mass ($m^*$) can also be achieved at the same point.[103]

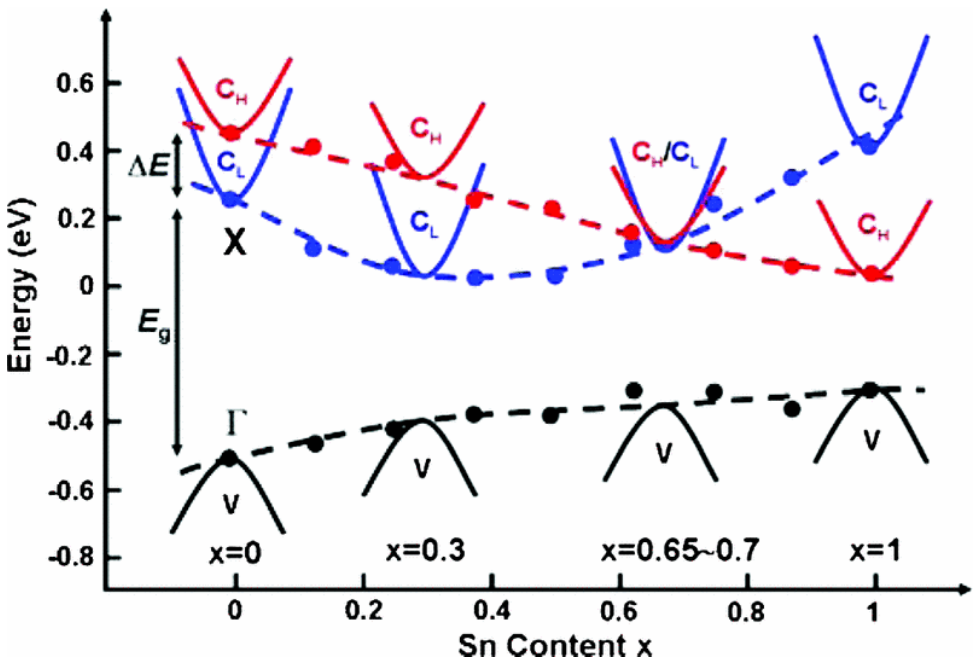


Figure 11. Band structure of $Mg_2Si_{1-x}Sn_x$ solid solutions.[103§]

The material can also be tuned with *p*-type doping. There are two kinds of *p*-type dopants, the first kind was used to substitute Mg, and the second kind was used to substitute Si. Some typical elements for the first kind include sodium (Na), potassium (K), lithium (Li), and silver (Ag), while gallium (Ga) was usually employed as the second kind of *p*-type dopant. Between all the first kind *p*-type dopants, lithium (Li) is the most efficient one, yielding a high electrical conductivity Li-doped $Mg_2Si$ of approximately 1100 $\Omega^{-1}cm^{-1}$.[87] The reason behind this is the similar radius that $Li^+$ (0.73 Å) has compared to $Mg^{2+}$ (0.71 Å).[104] Dopants with larger radius will presumably either occupy the octahedral holes directly, or boost magnesium into the octahedral holes, and will in turn lower the concentration of positive charge carriers. According

§ Reprinted with permission from (W. Liu, X. Tan, K. Yin, H. Liu, X. Tang, J. Shi, Q. Zhang, and C. Uher, Phys. Rev. Lett. *108*, 166601, **2012**) Copyright (2012) by the American Physical Society. http://dx.doi.org/10.1103/PhysRevLett.108.166601

to first principle calculations, Ag-doped $Mg_2Si$ revealed a preference of Mg occupying interstitial sites and became $Mg_I$ defects.[105] Thus Ag-doped $Mg_2Si$ exhibits a lower charge carrier concentration with a lower electrical conductivity.[73,106] With Ga being the dopant, first principle calculations revealed a Fermi level that is closer to the valence than in the undoped material, and the calculation results correspond well with the experimental results when Ga was employed in doping $Mg_2Si$ and $Mg_2Si_{1-x}Ge_x$.[107] Even though $Ga^{3+}$ has a similar radius (0.61 Å) compared to $Mg^{2+}$, Ga was a preferred substitution for Si rather than for Mg, which is mainly because of the low required formation energy with Ga.[108] After all, lithium (Li) doped material still possessed the highest positive charge carrier concentration of around $4.9 \times 10^{20}$ $cm^{-3}$, but the disadvantage of adding lithium is the instability issue under high temperature, which is due to the movement of lithium ions.[87]

Undoubtedly, antimony (Sb) and bismuth (Bi) are considered the most efficient *n*-type dopants. The carrier concentration increases significantly with the presence of antimony and bismuth, and consequently, the electrical conductivity is increased.

As a result of the high affinity of Mg with oxygen, one typical problem happened during the synthesis and characterization of *n*-type $Mg_2Si$ based material, is the presence of magnesium oxide (MgO) as impurity.[109–116] The presence of MgO in grain boundary may possibly improve the scattering process, but MgO also has low electrical conductivity,[117] and high thermal conductivity,[118] which will lower the efficiency of the energy conversion. Removing the MgO impurity is required to ensure a better performance of $Mg_2Si$ based thermoelectric materials.

Besides doping with heteroelements, experiment results revealed that the performance can be improved with the addition of Mg.[110,112,113,119–122] The charge carrier concentration can be

increased with excess Mg occupying the octahedral holes, and creating point defect scattering to decrease the thermal conductivity.[112,121,122]

Porous material was also investigated, and a high *ZT* value of 1.63 was achieved with Sb-doped $Mg_2Si_{0.5}Sn_{0.5}$ using pressure-less spark plasma sintering (SPS).[123] The porosity reduced the thermal conductivity significantly and, consequently, the figure-of-merit value increased. However, the porosity reduces the mechanical strength dramatically, which makes the material not appropriate for almost all applications. Moreover, further heat treatment would also modify the level of porosity, therefore affecting the properties. There is also a weak reproducibility for the porous sample, as the porosity level could not be controlled precisely.[123]

### 1.7 Other Group 2 Thermoelectric Silicides

Besides magnesium, some other elements from the same group can also form silicides with high potential as thermoelectric materials.

Calcium can form various binary compounds with silicon, such as $CaSi_2$ and $Ca_2Si$. $CaSi_2$ exhibits a high thermodynamic stability, and a good resistance to moisture, which makes the material more durable and stable under different conditions. Under a high pressure of 15 GPa, a phase transition was revealed for $CaSi_2$, and the material then possesses the properties of a superconductor under a low temperature of 14 K. $Ca_2Si$, a *p*-type semiconductor, has a carrier concentration of $3.1\times10^{16}$ $cm^{-3}$, and a band gap around 0.3 eV.[124–128] The material can also be tuned by adding Na, which will boost the carrier concentration by around a factor of 2 to around $1.3\times10^{18}$ $cm^{-3}$. The $Ca_2Si$ based material has a high Seebeck value (*S*) of approximately 200 μV $K^{-1}$.[128] $Ca_2Si$ was mainly considered for room temperature thermoelectric applications. On the

other hand, $Ca_3Si_4$ can be safely operated under medium temperature until its decomposition around 1183 K.

Similar to calcium, strontium can also combine with silicon, and form silicides for thermoelectric purposes. Research was conducted by adding aluminum (Al),[129] germanium (Ge),[130] yttrium (Y),[131] calcium (Ca),[132] and barium (Ba),[132] into the $SrSi_2$ based material. By doping with yttrium (Y), the $SrSi_2$ based material comprises the best *ZT* value of 0.4 under 300 K.[131]

### 1.8 Challenges and Motivations

Overall, magnesium silicide based and some other silicides based materials have great potentials as promising thermoelectric material. Most of the compositions are widely available, nontoxic (except for some trace amount dopants), and low-cost elements. The optimized synthesis is challenging mainly because of the combination of highly volatile Mg with relatively refractory Si. In addition, to optimize the thermoelectric performance selective isovalent (alloying), as well as aliovalent (doping) substitutions are the most conventional approaches, but such chemical manipulations are also challenging for $Mg_2Si$. This is due to either competitive formation of thermodynamically stable binaries ($Mg_3Bi_2$), or to the high (cubic) symmetry of the crystal structure of the pristine $Mg_2Si$, which is very sensitive to local symmetry breaking, and therefore not suitable for high concentration of point defects.

The choice of the alloying/doping element is also critical. Even in the case of isovalent substitution, a too large difference in atomic properties like electronegativity, size, and frontier

orbitals' energy, may result in a too high fluctuation of the atomic site energy, which has a destabilizing effect on the structure's stability.

With the challenges addressing above, my research was conducted around two major focuses: the first one was the synthesis procedures, and the second one was improving the performance through isovalent and aliovalent substitutions.

## 2.0 Experiment Procedures

There are certain procedures in synthesizing and optimizing magnesium silicide materials; all of them are essential to research on thermoelectric magnesium silicide. It is important to be familiar with the basic principles associated with laboratory operations, and to eliminate errors during characterization and ensure the quality of synthesized product

### 2.1 Synthesis

As previously mentioned, one of the major challenges exists in the synthesizing of $Mg_2Si$ based material. To overcome the issue and find the most efficient synthesizing method, different strategies were employed in my research, including solid state reaction, mechanical alloying, and $B_2O_3$ flux method. The general procedures will be introduced, and the advantages and drawbacks of different methods will be discussed.

The expectation from the synthesizing method is not only to produce material with the desired stoichiometry, but also to satisfy the needs from industry. Being environmental friendly and cost efficient, $Mg_2Si$ based thermoelectric material has a great potential to be employed for industrial applications, which means a larger batch size is required.

#### 2.1.1 Solid state reaction

##### 2.1.1.1 Principle of solid state reactions

Among all the synthesis methods, one of the oldest, simplest, also most common method is solid-state reaction. During solid state reactions, reactants will come in contact with each other, and products will be formed beginning at the interface between different reactants.[133] The principle of solid state reaction can be illustrated using one of the Escher paintings (Figure 12),

two different reactants (fish and birds) get in contact with each other under solid state reactions, and on the contact surface, the layer shows features from both fish and bird, but is not completely the same to either side.

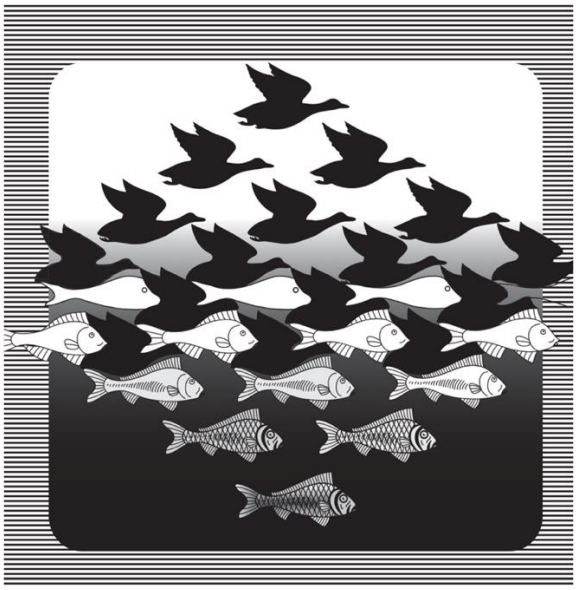

Figure 12. Escher painting: fishes to birds.[133**]

The speed of the reaction depends largely on the diffusion rate of the reactants, and solid-state reactions are usually slow, even with the particles are already well mixed, but the atoms are not excited and not ready to move towards homogeneity. To trigger the reaction, atomic level diffusion is required, and the most important two factors about diffusion are the reaction temperature and the diffusion path. When the temperature is insufficient, the energy input is not

** Reprinted with the permission from (Anthony R. West, Solid State Chemistry and its Applications, 2nd Edition, Student Edition, Wiley Books, John Wiley and Sons) copyright (2014)

enough to meet the requirement for effective diffusion, and an elevated temperature is usually required. Apart from the reaction temperature, the diffusion path length also has a huge impact on reaction speed, a shortened diffusion length can significantly reduce the solid-state reaction time, and reaction with only high temperature has its risk bring defects into the product. To reduce the diffusion path length, the sample can be pre-ground and pre-mixed, sometimes even compressed before solid state reaction. To further reduce the diffusion length, several reactants can be melted to create a liquid-solid mixed phase to create more effective contact area, in which case the solid reactants were surrounded by liquid reactant, the liquid-solid mixture can also enhance the reaction rate by reducing the diffusion length. To achieve a better homogeneity, the solid-state reaction can also be broken down into different steps, proceeding together with re-grinding, compressing, and re-heating, also known as annealing. The combination of different synthesis techniques may improve the purity and the homogeneity of the product significantly.

#### 2.1.1.2 Reaction containers for solid state reaction

The reaction container also plays an important role producing the product. Different containers have their own benefits and drawbacks, but there are certain general rules to follow when choosing the container. First, the container should stay inert to the reactant, avoiding to bring in any possible contaminations. Secondly, the container should be able to withstand the elevated temperature that is required for the solid-state reaction. Lastly, the container should also be cost-efficient. Based on the properties of the reactant, and different heating profiles, various types of reaction containers were used in our laboratory, including vacuum sealed silica ($SiO_2$) tubes, carbon coated sealed silica tubes, alumina ($Al_2O_3$) tubes, alumina crucibles or boats,

tantalum (Ta) tubes; sometimes niobium (Nb) foils and tantalum foils were also used to shape a suitable reaction container.

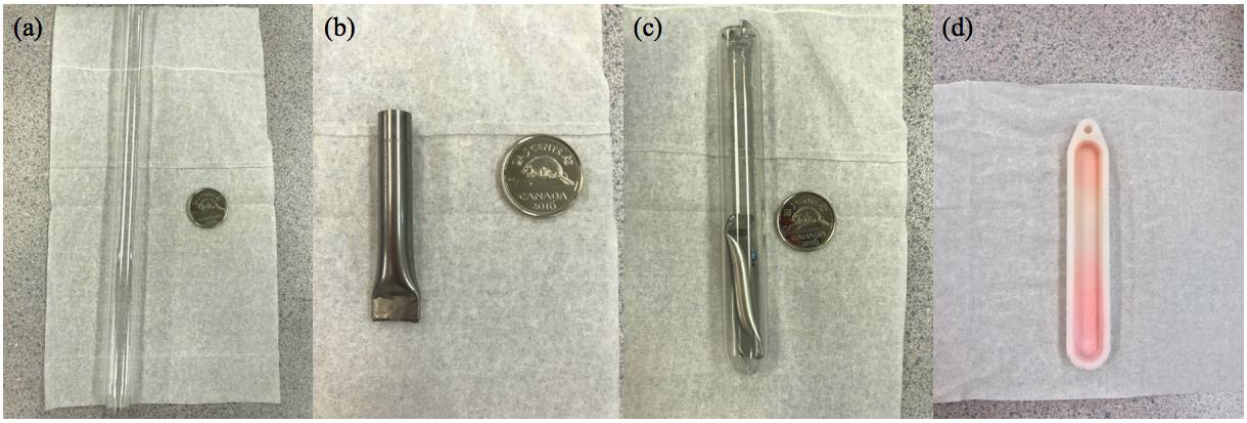


Figure 13. Reaction containers: (a) silica tube, (b) tantalum crucible, (c) sealed tantalum crucible in sealed silica tube, (d) alumina boat.

Silica tubes were used for most of the reactions in this laboratory, as the silica tubes can be made with customized volumes, the silica tube has a high melting point of around 1983 K, and can be evacuated using a vacuum line (Figure 14a), and sealed under vacuum using a hydrogen-oxygen torch (Figure 14b). The evacuated tubes provide a stable and oxygen free environment, which is beneficial to oxygen sensitive reactants. Alumina tubes, boats and crucibles are also used for reactions that could not be performed using silica tubes.

One drawback is the high cost for alumina tubes. Therefore, efforts were made to re-use the alumina tubes multiple times, but the risk of getting contaminations also increased along with reusing the containers. Tantalum crucibles were used for reactions containing volatile reactants. Tantalum has a high melting point of 3290 K, and can be welded using electric arc melting (Figure 15) to create a sturdy seal. Then the volatile reactants can stay enclosed during the

reaction without escape from the container and lose the stoichiometry, even under elevated temperature. During the arc melting, a high voltage arc is generated out of a tungsten electrode, with a strong current applied. The temperature varies, depending on the current passing through, and can be as high as 3300 K. However, due to the extremely high temperature, powders are not suitable because of their large surface area, which can enhance the risk of oxidization. Instead of powder, chunks, chips, and ingots are usually used for arc melting. The whole arc melting process should be carried out under a continuous argon flow, with cooling water turned on at a steady rate. In order to remove all the oxygen inside the arc melting chamber, a zirconium piece is usually arc melted two to three times in priority to arc melting.

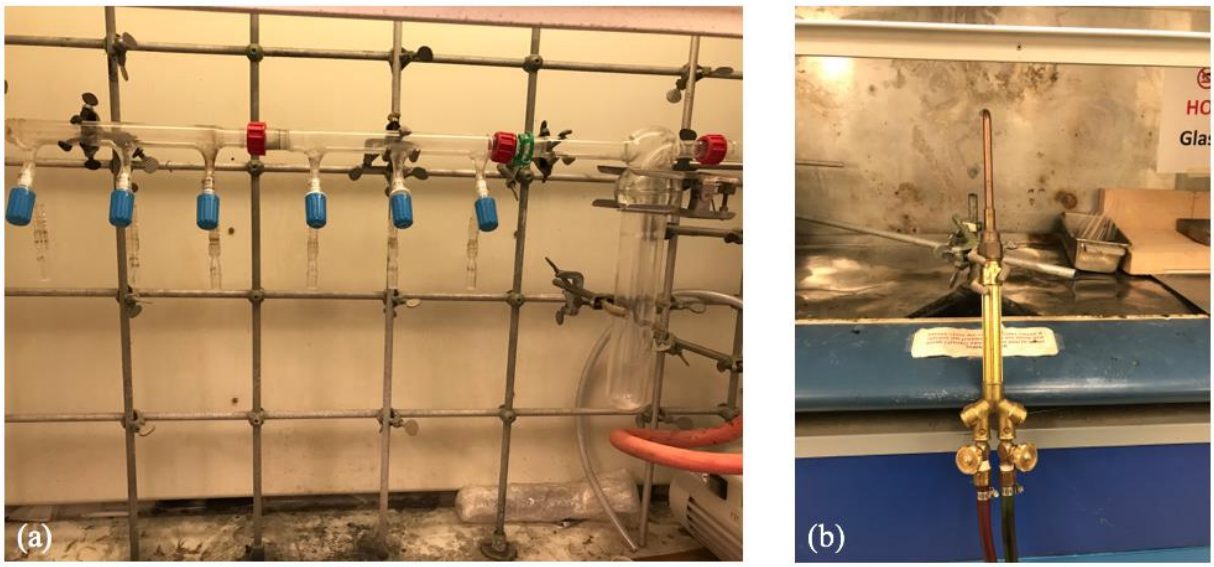


Figure 14. (a) vacuum line, (b) hydrogen-oxygen torch.

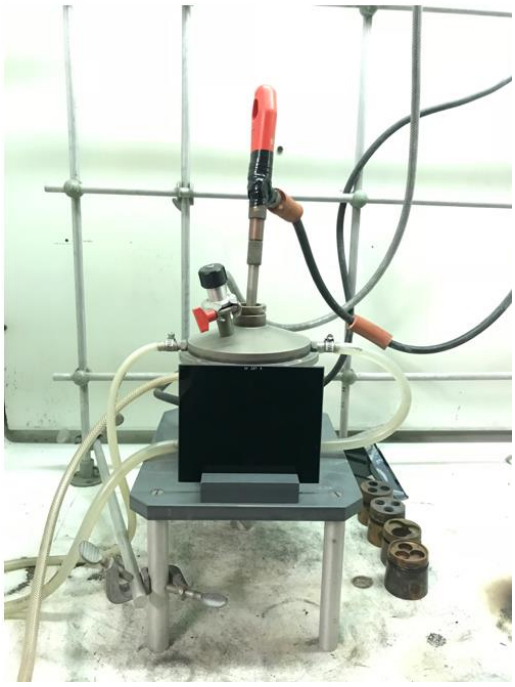

Figure 15. Arc melting set up.

### 2.1.1.3 Reaction containers for $Mg_2Si$ based materials

$Mg_2Si$ based thermoelectric materials were successfully synthesized using tantalum crucibles previously.[134] The starting materials were weighted according to stoichiometry in an argon-filled glove box (Figure 16), mixed and placed inside tantalum crucibles. The loaded tantalum crucibles were then transferred and sealed. After arc-melting, the tantalum container was placed inside a silica tube, then the silica tube was sealed under vacuum with an internal pressure around $2.5 \times 10^{-3}$ mbar. After the preparation, the sample was then moved for the solid state reaction into a muffle furnace (Figure 17).


Figure 16. Argon filled glove box.

Although tantalum crucibles have been proved to be one of the most practical containers for solid state reactions, the applications of tantalum crucibles are still limited by the high costs, and with welding and cutting, the physical strength of tantalum drops dramatically, making it remarkably hard to re-use the containers after the first reaction. Only tantalum tubes with small diameters can be sealed, which also limits the batch size to around two grams of product in each crucible.


Figure 17. Muffle furnaces: automated (left), manual (right).

For the above reasons, tantalum can be considered an excellent choice, but not necessarily the best. To solve these problems, different containers were tested. To replace the tantalum with a cheaper candidate, alumina crucibles were used first, but that was not suitable for reactions containing magnesium, as magnesium has a higher affinity to oxygen compared to aluminum, and under high temperature, the alumina crucible was reacting with the raw materials. The same problem occurred with fused silica tubes as well, which means for reactions containing magnesium, any type of direct contact between the raw materials and an oxidic container should be avoided, and an inert separation layer is required. Niobium foil (Figure 18) was tested at the beginning, but considering niobium foil has an even higher unit cost compared to tantalum crucible, the objective of reducing the cost was not achieved. The niobium foil also possessed limited flexibility, which made it difficult to be shaped to fit into different types of containers.


Figure 18. Niobium foil.

To find a better foil material, graphite considered next. The graphite foil (Figure 19a) can stay stable under high temperature, and remain inactive with Mg. Moreover, the foil is thin and soft by itself, and can be shaped to fit into the container. For the synthesis of $Mg_2Si$ based materials, the foil was wrapped to form a small cylinder that can be placed inside a silica tube (Figure 19b). To avoid the volatilization of magnesium under vacuum, the silica tube was left one-end open to maintain the standard atmospheric pressure. Raw materials were weighed, mixed, and loaded into the container in the glove box, and then transferred into a tube furnace purged with continuous argon flow (Figure 20) for heat treatment.

The advantages for solid state reaction include the straight forward process, the high yield, and the cost-efficient design. The customized container reduced the cost significantly comparing to the previously utilized tantalum crucible. The drawback for this method is the long annealing time required for the solid state reaction, which often takes from severval days to weeks.

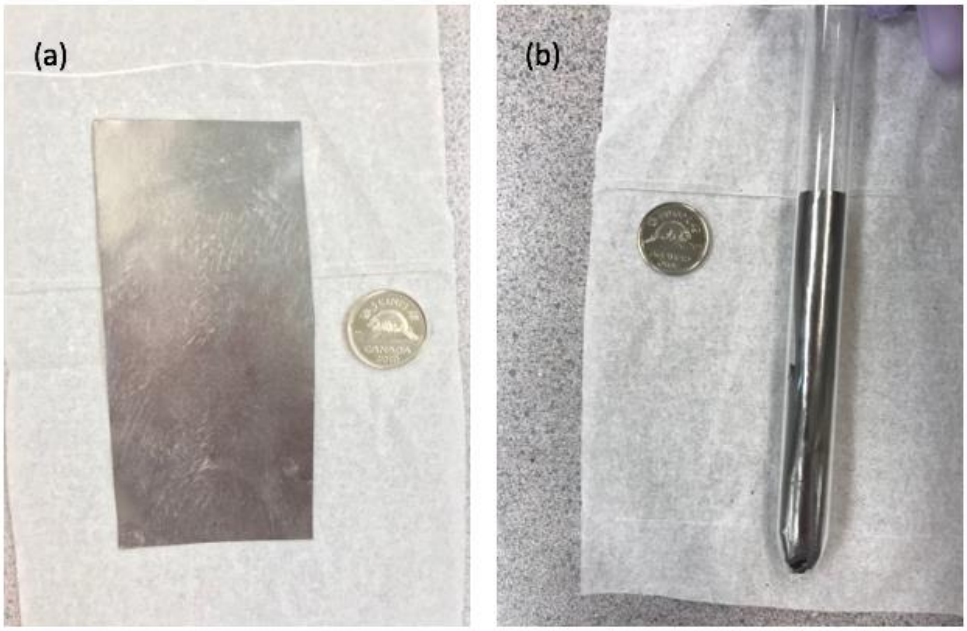


Figure 19. (a) graphite foil, (b) customized container.


Figure 20. Tube furnace with argon flow.

After reaction, the sample was taken out. An ingot was formed at the bottom of the container (Figure 21), and graphite was gently removed from the surface.


Figure 21. Product after reaction.

### 2.1.2 Mechanical Alloying

Mechanical alloying has been proven to be efficient in enhancing thermoelectric materials, which can be performed by planetary ball mills (Figure 22). The planetary ball mill is so named because of the special planet-like movement.[135] The vials are rotated around their own central axis, because of a special disk arrangement. The impact on materials and balls inside the system is provided by the centrifugal force. Because the vial rotates in an opposite direction as the disk, the centrifugal force changes its direction continuously, which causes the friction effect, and grinding balls slide down along the inner wall, collide and grind freely inside the vial (Figure 23). During continuous grinding, the energy is transformed from kinetic energy to chemical energy.[135] Thus the mechanical mill process is more suitable for brittle materials, as the impact from balls can be easily transferred.[136] In our case, magnesium is relatively soft, and tends to

deform under impact instead of getting fractured, which will lead to aggregation of magnesium at the inner wall of the ball mill chamber, hence resulting in non-stoichiometric, Mg-poor products.


Figure 22. Fritzsch ball mill machine.

One potential solution is using milling media, such as n-hexane to reduce the stickiness of magnesium, but this might in turn lead to organic impurities in the product.[137] To solve the problem, a so called “incremental milling” was proposed by Dr. Bux: during the mechanical alloying of bismuth doped $Mg_2Si$, by taking the silicon as milling aid, magnesium turnings were added gradually until the stoichiometric amount was reached, while the initial silicon and bismuth amounts were based on the final product.[136] After 8 - 10 hours, blue $Mg_2Si$ powder product was observed, and the amount was 4 to 10 grams per batch. The advantage of this method is the short processing time, and the drawback is the poor control of the side products, as frequently opening and adding material into the reaction chamber might introduce contaminations.

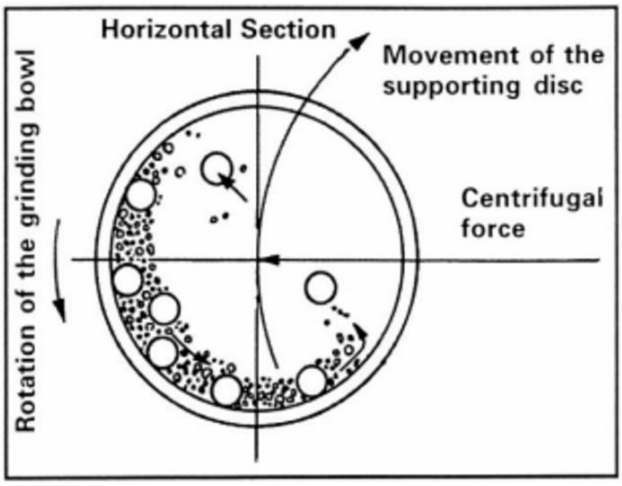


Figure 23. Schematic of ball mill motion inside the jar.

### 2.1.3 Boron oxide flux synthesize method

A flux method using $B_2O_3$ for synthesizing magnesium silicide material was introduced in 2011.[138] At high temperature, the $B_2O_3$ flux functions as a liquid seal to separate the raw materials from the air, so that the oxidation of magnesium is reduced or even completely inhibited.[138] For the flux method, raw materials were weighed and mixed in a glove box, then transferred into alumina crucibles. Graphite foils were also used to separate the raw material from the $B_2O_3$ powder. The loaded alumina crucibles were transferred into a preheated furnace for annealing. After annealing, the final product was removed. The removal method was not mentioned in the publication, but apparently the alumina crucible was smashed into pieces to get the sample out. A hot-pressing procedure was applied afterwards. The advantage of the flux synthesis is the short processing time and straight forward process. The drawback is the difficulty in separating product and the flux. The physical separation will result in severe damage

to the container, which increases the cost dramatically, while the chemical separation might damage the product.

There were also other approaches reported with success on the synthesis of $Mg_2Si$ based thermoelectric material. Because of the limitation of time and equipment, only the methods mentioned here were attempted, and the solid-state reaction was chosen as the preferred synthesis method in this thesis.

## 2.2 Characterization

### 2.2.1 Powder X-ray diffraction analysis (P-XRD)

P-XRD is a technique used wildly in characterizing the crystal structure of an object, and phase identification of the synthesized material. The INEL XRG 3000 powder diffractometer with a copper- Kα1 radiation was used in this research (Figure 24).

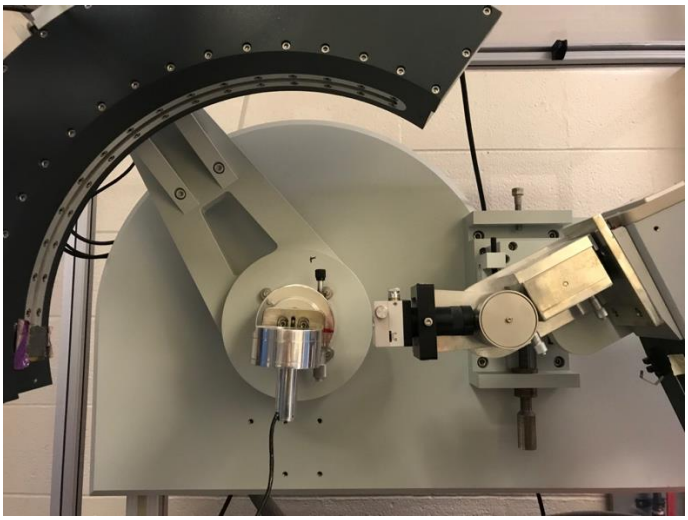

Figure 24. INEL XRG 3000 powder X-ray diffractometer.

The functioning principle of X-ray diffraction machine can be described as the following: heating a tungsten filament generates electrons, and those electrons are accelerated by a high voltage of 30 kV in our case. The high-speed electrons bombard a copper anode, kicks one of the inner shell electrons out, and creates a vacancy. The created vacancy would be filled by an electron from the outer shell, and generates an inequivalency in energy. Any extra energy would be emitted in the form of X-rays. X-rays being generated vary in wavelength, which depends on the material used. In order to produce a monochromatic beam of X-rays, a monochromator made of a germanium crystal is applied in our setup.[139]

X-rays interfere with electrons either constructively or destructively (Figure 25). Referring to Bragg's law (Equation 11), if the difference between the lengths of two beams' pathway equals to an integer number of the wavelength of the X-rays, the interference is constructive., Otherwise the interference is destructive, and only the constructive interaction can be observed and recorded.

$$n\lambda = 2d\ sin\theta \qquad \text{Equation 11}$$

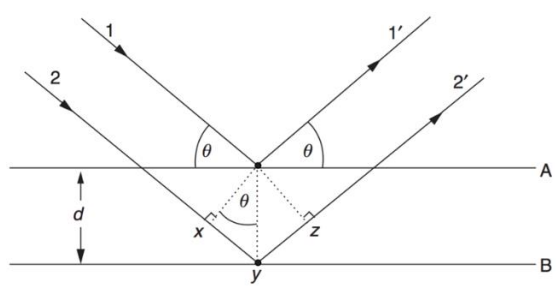


Figure 25. Constructive X-ray interference,1 and 2: incident beams, 1′ and 2′: reflected beams

To characterize a product using the powder X-ray diffraction machine, the product must be ground into fine powder to achieve the maximum number and random orientations of crystals. In this research, the annealed product was ground using mortar and pestle (Figure 26). The X-ray machine was run for at least thirty minutes to determine the phase purity.

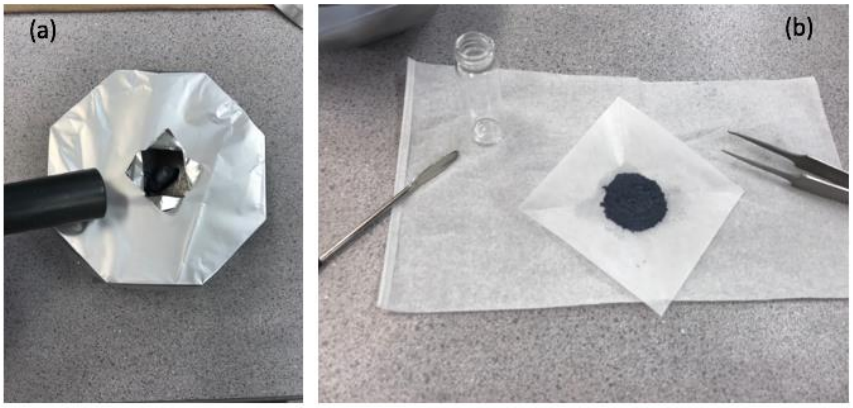


Figure 26. (a) Mortar and pestle, (b) grounded product

### 2.2.2 Consolidation

After examining the purity of a synthesized sample, the next step was consolidation. The consolidation process took place in the Oxy-Gon hot-press machine (Figure 27). During the consolidation, high pressure and high temperature was applied at the same time, with the sample being pressed in a graphite die. The energy was transferred from the tungsten heating elements to the sample, and the temperature was set below the melting point of the product. The force was applied vertically via two specifically strengthened graphite rods, with an upper limitation of 30 tons. During the hot-pressing process, the sample forms a thin pellet with a diameter of 12.7 mm

and a height of 2 - 4 mm (Figure 28). To ensure the absence of any undesired oxygen inside the pressing chamber, the whole pressing process is carried out under inert gas flow.


Figure 27. Hot-press instrument.

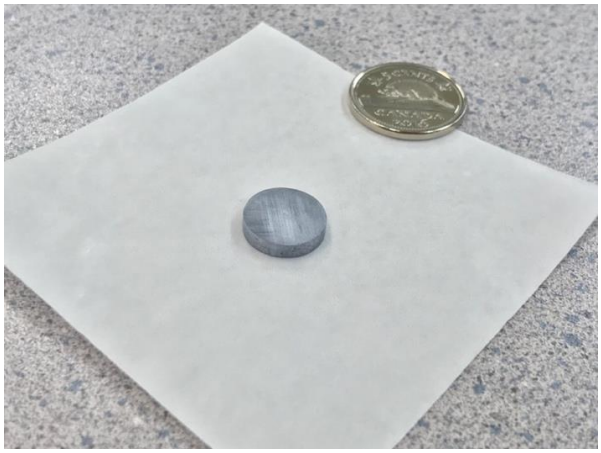

Figure 28. Pressed sample

### 2.2.3 Density measurement

The density of sample was measured after densification, and the Archimedean method was used. The Sartorius YDK01 density kit (Figure 29) was employed for this measurement. By immersing the pressed disk into the reference liquid (distilled water or ethanol), the weight of the sample would be decreased by a certain amount, which is the same as the weight of the liquid being displaced by the sample. The density can be determined using the following equation:

$$d_{solid} = \frac{m_{air} \times d_{liquid}}{m_{air} - m_{liquid}} \qquad \text{Equation 12}$$

Where $d_{solid}$ is the density of sample, $m_{air}$ is the weight of sample measured in air, $m_{liquid}$ is the weight of sample measured in liquid, $d_{liquid}$ is the density of the reference liquid.

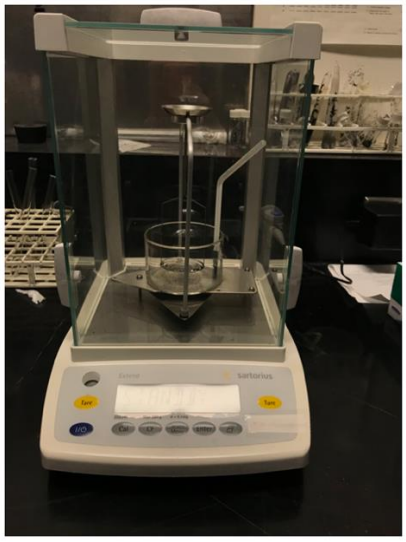

Figure 29. The Sartorius YDK01 density kit.

However, the accuracy from this equation is not enough, as there are other factors that need to be evaluated, such as the influence of the temperature on the density of the reference liquid, the volume of the measurement kit immersed in the liquid, and the possibility of air bubbles on or in the sample.

To eliminate the error caused by the fluctuation of temperature, the real time temperature need to be recorded during measurement, and a corresponding $d_{liquid}$ should be chosen accordingly. Moreover, for distilled water, the change in every degree is around 0.02%, and the change is 0.1% for ethanol. Therefore, distilled water is the preferred reference liquid unless in case of water-sensitive samples.

The density of air was also considered as an error source, and the equation was further modified (Equation 13) to cancel this error out, with the density of air being 0.0012 g/cm$^3$.

$$d_{solid} = \frac{m_{air} \times (d_{liquid} - d_{air})}{m_{air} - m_{liquid}} + d_{air} \qquad \text{Equation 13}$$

A correction coefficient of 0.99983 was added to the denominator to fix the impact from the partially immersed density kit, with the formula being modified to:

$$d_{solid} = \frac{m_{air} \times (d_{liquid} - 0.0012)}{0.99983 \times (m_{air} - m_{liquid})} + d_{air} \qquad \text{Equation 14}$$

To get rid of adhesive air bubbles, the sample was examined carefully before being immersed into the liquid. Sometimes the sample was immersed in the reference liquid in a different container before the actual measurement.

### 2.2.4 Thermal Diffusivity Measurements

Thermal diffusivity measurements can be performed on the pellet prepared in the hot-press. During the measurement, the bottom surface of pellet will be struck by an intense beam of a xenon flash. The heat will then propagate through the pellet to the top surface. The temperature of the top surface will change accordingly to the energy absorbed, and the difference in temperature will be detected by an infrared (IR) detector (Figure 30).[140] During the whole measurement, the furnace chamber is under argon, to avoid any oxidation.

The expression used to determine the thermal diffusivity is shown below: [141]

$$\alpha = c \times l^2 \times t_{0.5}^{-1}. \qquad \text{Equation 15}$$

Based on this equation, the thermal diffusivity can be determined by multiple parameters including thickness $l$, half time $t_{0.5}$, and the constant $c$. In order to perform a precise measurement, one needs to precisely determine the thickness of the tested sample. Moreover, coated graphite layers on the top of both surfaces are necessary to reduce the error caused by reflection. After the measurement, the thermal conductivity can be calculated based on the expression provided below: [141]

$$\kappa = \alpha \cdot \rho \cdot C_p. \qquad \text{Equation 16}$$

$\kappa$ is the thermal conductivity, $\alpha$ is the thermal diffusivity as measured, $\rho$ is density, and $C_p$ is the specific heat capacity, for example calculated with the Dulong-Petit approximation:

$$C_p = \frac{3R}{M}. \qquad \text{Equation 17}$$

Where $R$ is the gas constant and $M$ is the calculated average molar mass.

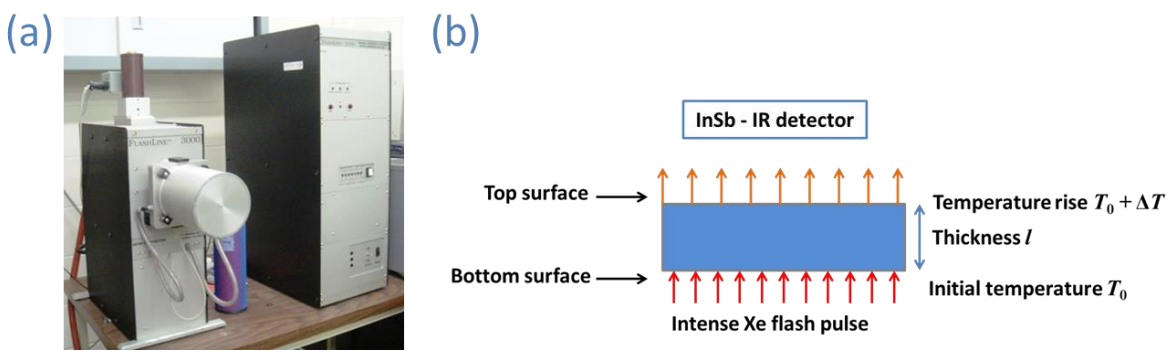


Figure 30. (a) Anter Flashline 3000; (b) Schematic of Flash Method Measurement.

### 2.2.5 Electrical Property Measurements

After the flash method is conducted, the sample will be prepared for electrical property measurements, performed by using the ULVAC-RIKO ZEM 3 instrument. The sample is cut into a rectangular bar with approximate dimensions of 2 × 2 × 10 mm, and placed between two electrodes, with a pair of thermocouples in contact on its side (Figure 31). The measurement process is carried out in a helium filled chamber, with temperatures ranging from room temperature to 800 K. To ensure the quality of contact, a $V$ (voltage) - $I$ (current) plot is drawn first.

Figure 31. ULVAC-RIKO ZEM3.

The measurement and calculation of the Seebeck coefficient can be performed by heating the bottom of the tested sample, with recording the difference in temperature between the two thermocouples. With measuring the voltage difference between the two thermocouples, the Seebeck coefficient can be determined as:

$$S = \frac{\Delta V}{T_1 - T_2}. \qquad \text{Equation 18}$$

The electrical resistivity ($\rho$) can be calculated based on the equation:

$$\rho = \frac{R \cdot A}{L}. \qquad \text{Equation 19}$$

$L$ is the distance between two thermocouples, $A$ is the sample's cross sectional area, and $R$ is the resistance, which can be determined by:

$$R = \frac{\Delta V}{I}. \qquad \text{Equation 20}$$

Respectively, the electrical conductivity can be determined with:

$$\sigma = \frac{1}{\rho}. \qquad \text{Equation 21}$$

### 2.2.6 Differential Scanning Calorimetry (DSC)

Differential Scanning Calorimetry (DSC) is a thermal analysis technique, during which the heating process of the sample is recorded and analyzed. Based on the achieved result, the melting point can be determined, and then the heating and annealing conditions can be configured and adjusted accordingly for the synthesis and hot-pressing process. However, a reference material is required for DSC measurements. DSC is processed by NETZSCH STA 409PC LUXX (Figure 32), with a possible temperature range from 300 K to 1900 K, and under inert argon atmosphere.

Figure 32. NETZSCH instrument for DSC.

### 2.2.7 Electron dispersive X-ray spectroscopy (EDX)

The energy dispersive X-ray spectroscope is used to estimate the elemental composition of the analyzed sample, and identify the presence of heteroelements, if any. During the EDX analysis, the sample will be exposed to a high energy beam, by which some electrons will be knocked out from the inner shell (Figure 33). Consequently, electrons from outer shell will then fall down to fill the vacant position. The migration of the electron from an outer shell to an inner shell will result in an energy difference. The energy difference will generate a characteristic X-ray, which can be analyzed to identify the element. To analyze the surface geometry of the analyzed sample, a scanning electron microscope is usually operated at the same time.


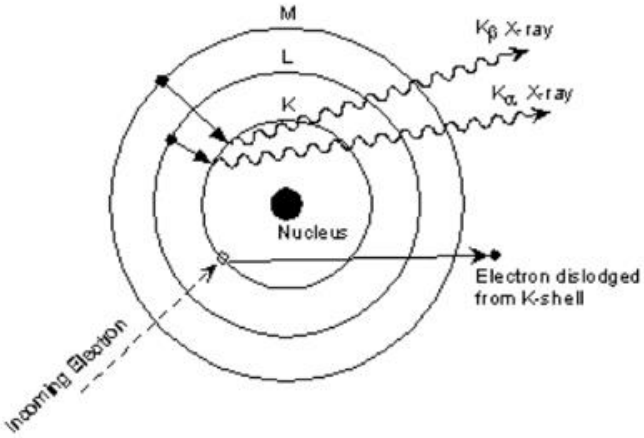


Figure 33. Quanta FEC 250 EDX machine (left), and working mechanism of EDX (right).

### 2.2.8 Density functional theory for energy band calculation

To calculate the electronic structures of various model compounds, the density function theory (DFT) was employed, using the software package WIEN2K.[142] In the case of $Mg_2Si$-$Mg_2Sn$-$Mg_2Pb$ solid solutions, a consistent supercell was used to simulate different Si/Sn/Pb ratios. It is worth noting that the band width from this calculation is usually underestimated, thus, corrections were made by applying the modified Becke and Johnson potential (mBJ) during the calculation.[143]

## 3.0 Results and discussion

### 3.1 Synthesis

The synthesis methods were discussed in previous chapters, and as specified, the solid-state reaction synthesis was employed as the primary synthesis method.

Samples were prepared from pure elements (Mg chips: Sigma Aldrich Chemistry, 99.98%; Si powder: Alfa Aesar, 99.9%; Sn granules: Alfa Aesar, 99.9%; Pb granules: Strem Chemistry, 99.99%; Bi granules: Sigma Aldrich Chemistry, 99.99%). A large quartz tube with an inner diameter of eight centimeters was used. To fulfill the requirement for large scale production, multiple tubes with samples inside were placed in the larger tube for heating treatment (Figure 34). With this arrangement, the estimated yield can be as high as 50 grams per batch, which is a large step towards fulfilling the needs from industry. During the reaction, the large quartz tube remains open, with argon being purged throughout the entire process.

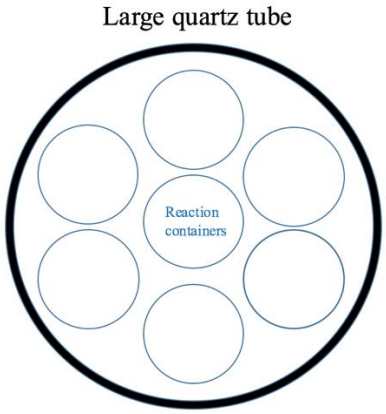


Figure 34. Arrangement of reaction containers in the large quartz tube.

To successfully synthesize the product, efforts were made tuning the heating profile. Magnesium is highly volatile; thus, a low synthesis temperature is more favorable to avoid the potential stoichiometry loss. Recent research reported successful synthesis with the help of mechanical milling, and with the annealing under 873 K for 1 hr.[144] Extrapolating the heating profile from the literature, the duration of annealing was extended without mechanical alloying, with 16 hours of annealing at 673 K, then 48 hours at 873 K, afterwards down to room temperature (RT) in 7 hours (Figure 35).

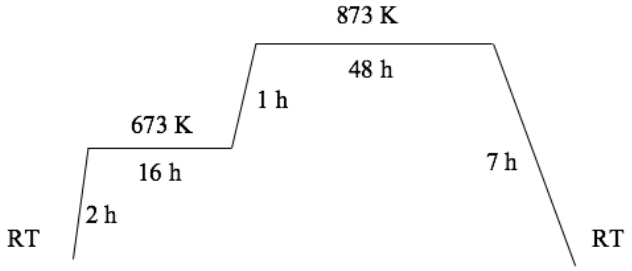


Figure 35. Heating profile extrapolated from literature.

However, with this profile, the attempts on obtaining single phase product were not successful; numerous impurity phases were reviewed in the products according to X-ray powder diagrams. The failures were mainly due to the relative low reaction temperature, as silicon has a high melting point around 1680 K. The literature reported 873 K, however, this was not sufficient to complete the reaction without the aid of mechanical alloying. Therefore, a higher reaction temperature of 1173 K was employed. The side phases were reduced to a minimum amount with only $Mg_2Si$, and regardless of the reaction time, $Mg_2Si$ always exists in the product. To understand the reason, the phase diagram presented in Figure 36 was reviewed.

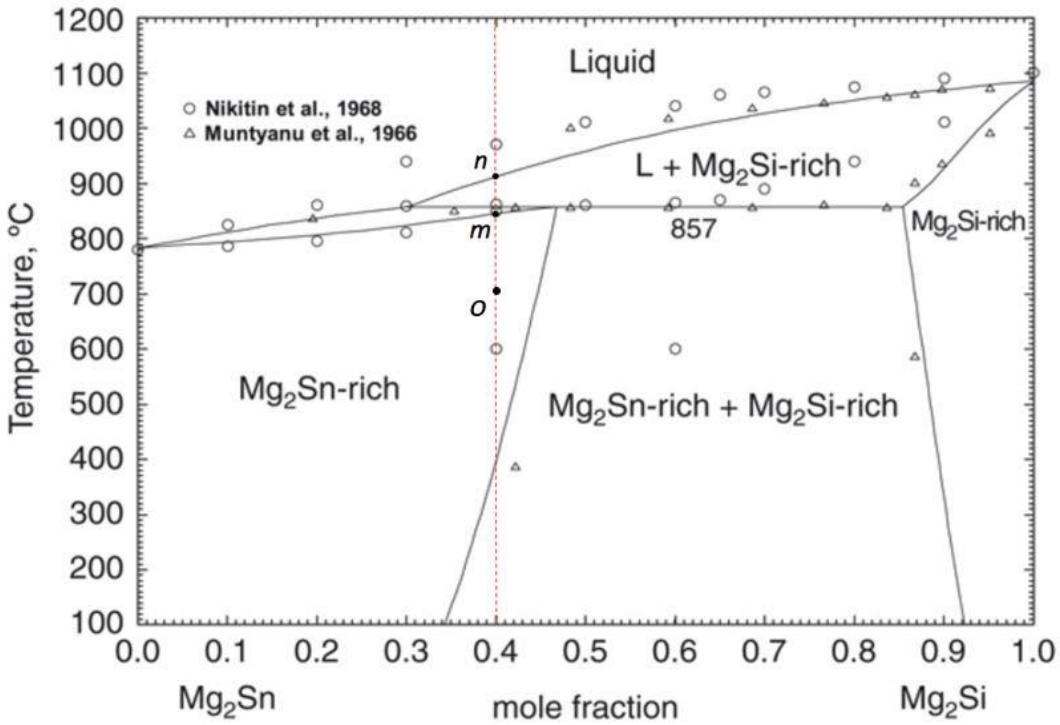


Figure 36. Phase diagram for Mg-Si-Sn system, adopted from [145].

Using the composition of $Mg_2Si_{0.4}Sn_{0.6}$ as an example (indicated by the red line), to achieve an efficient reaction, the previously used annealing temperature should be increased, to the point where the liquid - solid phase reaction can be triggered. In the case of $Mg_2Si_{0.4}Sn_{0.6}$, the annealing point should be at least above point *n* (1193 K, 920°C), and the previously employed temperature may have the risk of falling into the region with multiple stable phases (between *n* and *m*), and to bypass region *nm*, a fast cooling process is preferred. A test with a sealed tantalum crucible was conducted on a Bi-doped $Mg_2Si_{0.4}Sn_{0.6}$ sample, namely with an annealing temperature of 1223 K, a fast cooling down by water quenching, and finally a three-day annealing step at 973 K (point *o* in Figure 36), the modified heating profile is demonstrated in Figure 37.

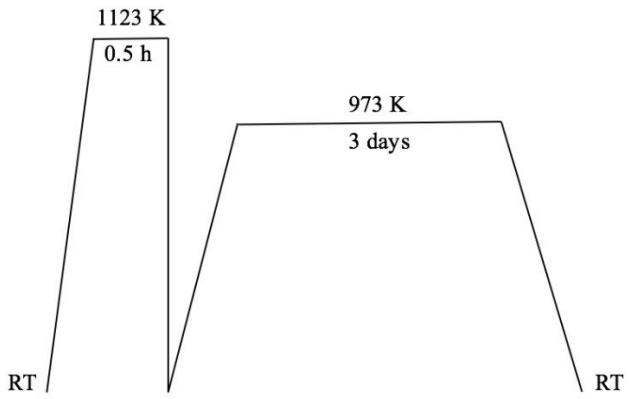


Figure 37. Modified heating profile with water quenching.

After reaction, the sample was retrieved, and ground into fine powder for powder X-ray diffraction analysis, and the result is shown in Figure 38, compared with the reference pattern of undoped $Mg_2Si_{0.4}Sn_{0.6}$ from ICSD #44934.[146]

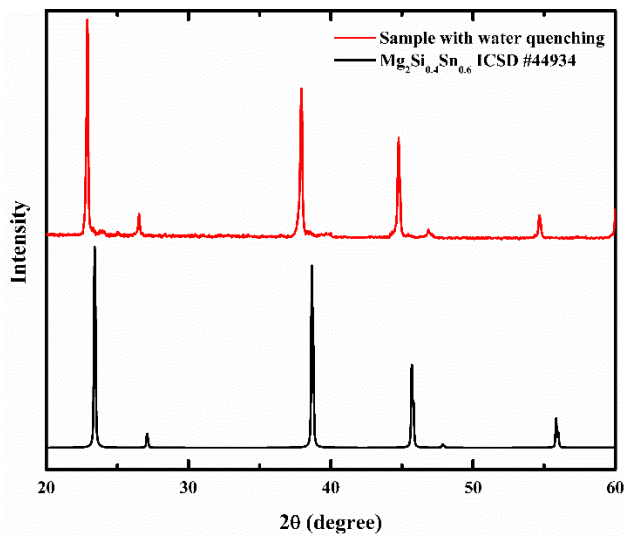


Figure 38. X-ray diffraction analysis for sample with water quenching.

From the X-ray diffraction result, we can conclude that the sample is almost pure, the positions for the major peaks correspond well to the reference with a systematically shift to the left, which was mainly due to the lattice expansion with the doping of Bi. Therefore, the result proves that a fast cooling process can facilitate the synthesis of single phase product. However, small shoulders were observed at 24º and 40º, which suggests an incomplete reaction. As a result, the heating profile needed to be further modified to achieve purer product if possible.

To achieve a more sufficient solid-liquid reaction, the annealing duration under 1223 K should be extended. Moreover, the water quenching process will not work for a reaction without a sealed environment. For the open tube used in this project, a fast cooling from 1223 K to 973 K in half hour was employed to simulate the quenching process. The efficiency of the second annealing at 973 K was also evaluated, and different durations were tested. The result is shown in Figure 399.

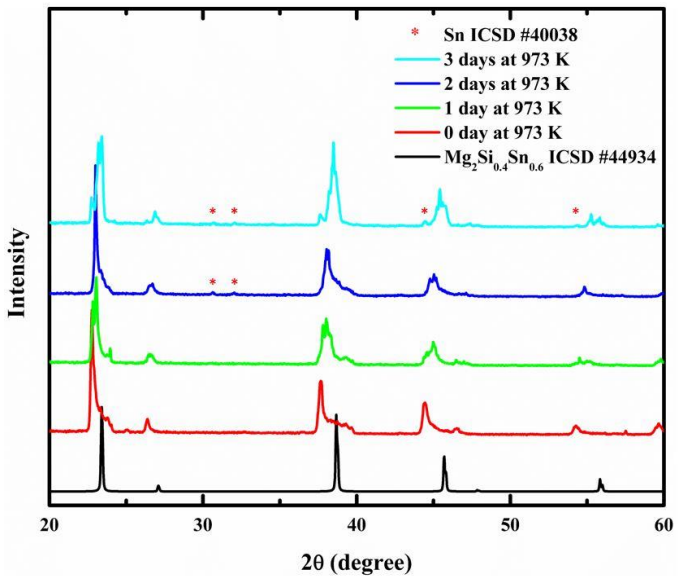


Figure 39. Bi-doped $Mg_2Si_{0.4}Sn_{0.6}$ samples with different annealing durations.

At this point, no single-phase product was obtained, but there is a trend in decreasing the level of phase segregation with a longer annealing duration. The secondary phase exists in the sample with two days and three days annealing, which was revealed to be tin (Sn) peaks in Figure 39. The presence of tin was mainly due to the magnesium loss under high temperature with long time annealing. To counter the loss, excess magnesium was added for the reaction with three days of annealing. After that, the sample was hot-pressed under the pressure of 60 MPa and a high temperature of 923 K. Thereafter, the sample with three days annealing at 973 K revealed to be single phase. An example is shown in Figure 40.

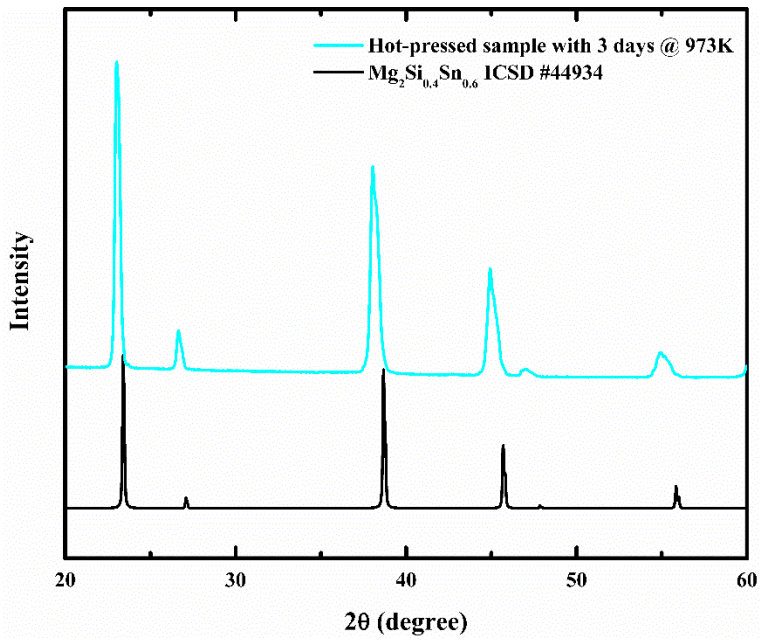


Figure 40. X-ray diffraction pattern for hot-pressed sample with three days annealing at 973 K.

The finalized heating profile was then applied, and all the work presented in this thesis hereafter was conducted using the same heating profile.

### 3.2 Enhanced performance of magnesium silicide-stannide based material

Magnesium silicide-stannide based materials with the best performances are listed in Table 1.

Table 1. Physical properties of magnesium silicide-stannide based thermoelectric materials

| **Composition** | **Seebeck (μV/K)** | **Thermal Conductivity (W/m·K)** | **Power Factor (μW/cm·K)** | ***ZT*** | ***T* (K)** |
|---|---|---|---|---|---|
| $Mg_{2.16}(Si_{0.3}Ge_{0.05}Sn_{0.65})_{0.98}Sb_{0.02}$[147] | 220 | 2.3 | 47 | 1.5 | 740 |
| $Mg_{2.16}(Si_{0.4}Sn_{0.6})_{0.97}Bi_{0.03}$[148] | 220 | 2.3 | 43 | 1.4 | 800 |
| $Mg_2Si_{0.3}Sn_{0.65}Bi_{0.035}$[58] | 220 | 2.3 | 43 | 1.4 | 773 |
| $Mg_{2.16}(Si_{0.4}Sn_{0.6})_{0.985}Sb_{0.015}$[113] | 240 | 2.1 | 37 | 1.3 | 740 |
| $Mg_2Si_{0.4}Sn_{0.6}Bi_{0.03}$[149] | 260 | 1.2 | 28 | 1.2 | 573 |

Excellent thermoelectric properties were revealed for Bi and Sb doped samples, and the sample composition is always around $Mg_2Si_{0.4}Sn_{0.6}$. Another way to improve the performance is by adding lead (Pb) into the bulk material; a research conducted in 2013 by Muthiah *et al*. suggested an increase in *ZT* from 0.03 to 0.56 with 2 atomic percent of lead being added into bulk $Mg_2Si$.[97] However, until recent, there is no work reported with Pb and Bi co-doping on $Mg_2Si_xSn_{1-x}$ solid solutions, which became the major focus of this research.

Unlike the doping with bismuth, the carrier concentration remains unchanged when lead is added instead. The enhancement in thermoelectric properties is mainly due to the phonon scattering by point defects introduced by the alloying, and as well as the increased structure

complexity. With enhanced scattering, the lattice thermal conductivity can be reduced significantly. Furthermore, as introduced in previous chapters, the band convergence is one of the reasons that enhanced the performance of $Mg_2Si$-$Mg_2Sn$ solid solution, and with the similar mechanism, it can be predicted that the $Mg_2Si$-$Mg_2Sn$-$Mg_2Pb$ system also shows band convergence, which would enhance the thermoelectric performance by enhancing the Seebeck coefficient without changing the electrical conductivity.

However, alloying introduces point defects which scatter phonons but also reduce the carrier mobility and subsequently the electrical conductivity. $Mg_2Pb$ with its small band gap exhibits a significant bipolar effect. In semiconductors with small band gaps, the intrinsic charge carriers can be easily bumped up into conduction band by thermal excitation, and result in the presence of both positive charge carriers and negative charge carriers.[150] The co-existence of different charge carriers lowers the Seebeck coefficient, as the *n*-type charge carriers contribute to a negative Seebeck, while *p*-type carriers contribute to a positive Seebeck coefficient.

For the above reasons, the doped products may not reveal better electrical properties compared to the Sb or Bi doped samples, but their thermal conductivities are expected to be lower than the sample without Pb doping. Hence, the amount of dopant needs to be optimized accordingly. Considering the large atomic radii of Pb and Bi, trace amount of dopant was employed. With a composition of $Mg_2Si_{0.4-x}Sn_{0.6-y}Pb_yBi_x$, with x fixed at 0.05, and y = 0, 0.03, 0.05, 0.07, 0.1.

### 3.3 Sample purity, lattice parameter, and density

After the solid state reaction, the samples were hot-pressed. Then the products were ground into fine powder, and their purity was examined with the aid of the X-ray diffraction machine (Figure 41).

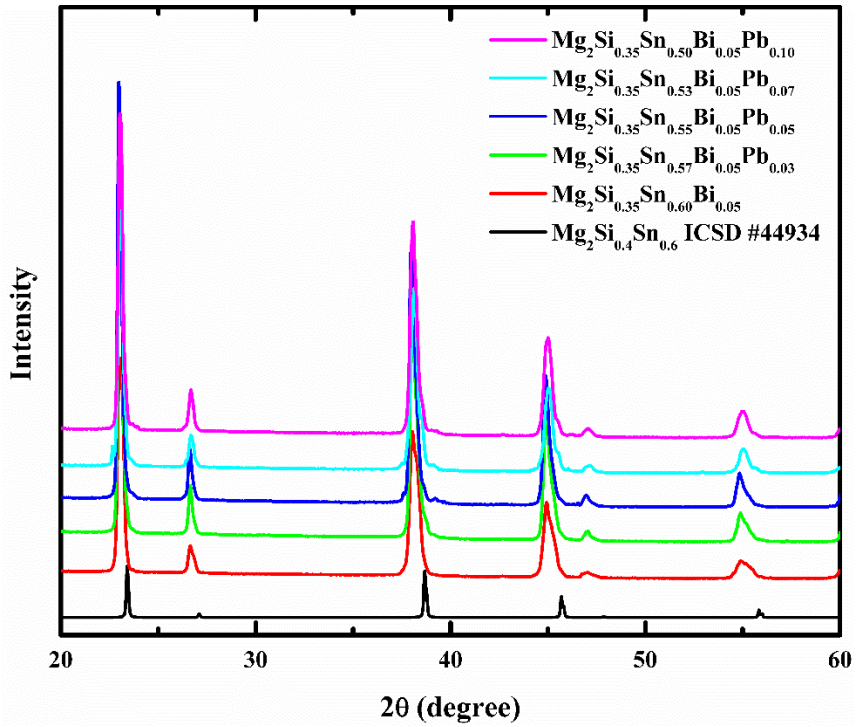


Figure 41. X-ray diffraction patterns of $Mg_2Si_{0.35}Sn_{0.6-x}Pb_xBi_{0.05}$ samples, with x = 0, 0.03, 0.05, 0.07, 0.10.

From the X-ray patterns, all examples were close to pure, with no MgO phase was revealed in the product.

Lattice parameters of selected samples were also obtained through refinement using the "Rietveld" program, and the results are in agreement with the expected lattice expansion.

Table 2. Lattice parameter refinements on selected samples.

| Composition | Lattice Parameter (Å) | Volume (Å$^3$) |
|---|---|---|
| $Mg_2Si_{0.35}Sn_{0.6}Bi_{0.05}$ | 6.6569 (6) | 295.0 |
| $Mg_2Si_{0.35}Sn_{0.57}Pb_{0.03}Bi_{0.05}$ | 6.6584 (7) | 295.2 |
| $Mg_2Si_{0.35}Sn_{0.53}Pb_{0.07}Bi_{0.05}$ | 6.6602 (2) | 295.4 |
| $Mg_2Si_{0.35}Sn_{0.5}Pb_{0.10}Bi_{0.05}$ | 6.6622 (4) | 295.7 |

### 3.4 SEM and EDX

One of the major concerns towards doped materials is the localization of the dopant in grain boundaries. To prove that uniform distributions were achieved for all the samples, EDX mapping and area scans were performed. Five areas for each sample were scanned for evaluation of composition, and the average was calculated to compare it with the stoichiometric value. However, with the limitation of the accuracy of EDX, errors exist in the analysis of the composition, and only the trend of the dopant amounts was compared. In the analyzed mapping pictures, Mg is represented in blue, Si in yellow, Sn in red, Pb in light gray, and Bi in green.

Table 3. Area scan results (percentages) of $Mg_2Si_{0.35}Sn_{0.6}Bi_{0.05}$ sample.

| Element | Area 1 | Area 2 | Area 3 | Area 4 | Area 5 | Avg. | Nominal |
|---|---|---|---|---|---|---|---|
| Mg | 65.5 | 66.3 | 66.3 | 66.4 | 67.5 | 66.4 | 66.7 |
| Si | 10.4 | 10.7 | 10.2 | 11.8 | 8.9 | 10.4 | 11.7 |
| Sn | 22.2 | 21.3 | 21.7 | 19.8 | 21.6 | 21.3 | 20.0 |
| Bi | 1.8 | 1.6 | 1.9 | 2.0 | 2.1 | 1.9 | 1.7 |

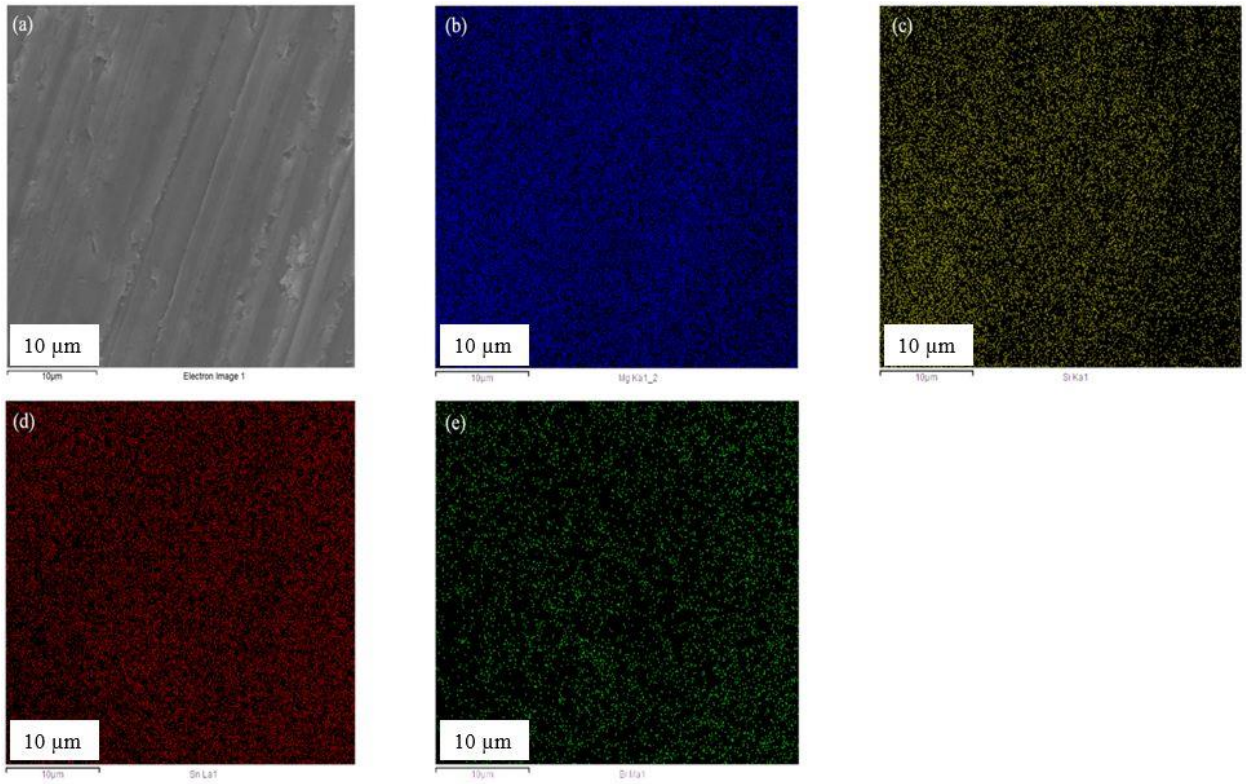


Figure 42. EDX mapping of $Mg_2Si_{0.365}Sn_{0.6}Bi_{0.05}$ sample, with (a) mapping area; (b) Mg; (c) Si; (d) Sn; (e) Bi represented by different colors.

Table 4. Area scan results (percentages) of $Mg_2Si_{0.35}Sn_{0.57}Pb_{0.03}Bi_{0.05}$ sample.

| Element | Area 1 | Area 2 | Area 3 | Area 4 | Area 5 | Avg. | Nominal |
|---|---|---|---|---|---|---|---|
| Mg | 66.2 | 66.5 | 65.7 | 66.3 | 66.3 | 66.2 | 66.7 |
| Si | 12.8 | 11.2 | 12.3 | 9.8 | 11.9 | 11.6 | 11.7 |
| Sn | 18.7 | 20.1 | 19.5 | 21.6 | 19.5 | 19.9 | 19 |
| Bi | 1.6 | 1.3 | 1.7 | 1.3 | 1.4 | 1.5 | 1.7 |
| Pb | 0.7 | 0.9 | 0.8 | 1.0 | 0.9 | 0.9 | 1.0 |

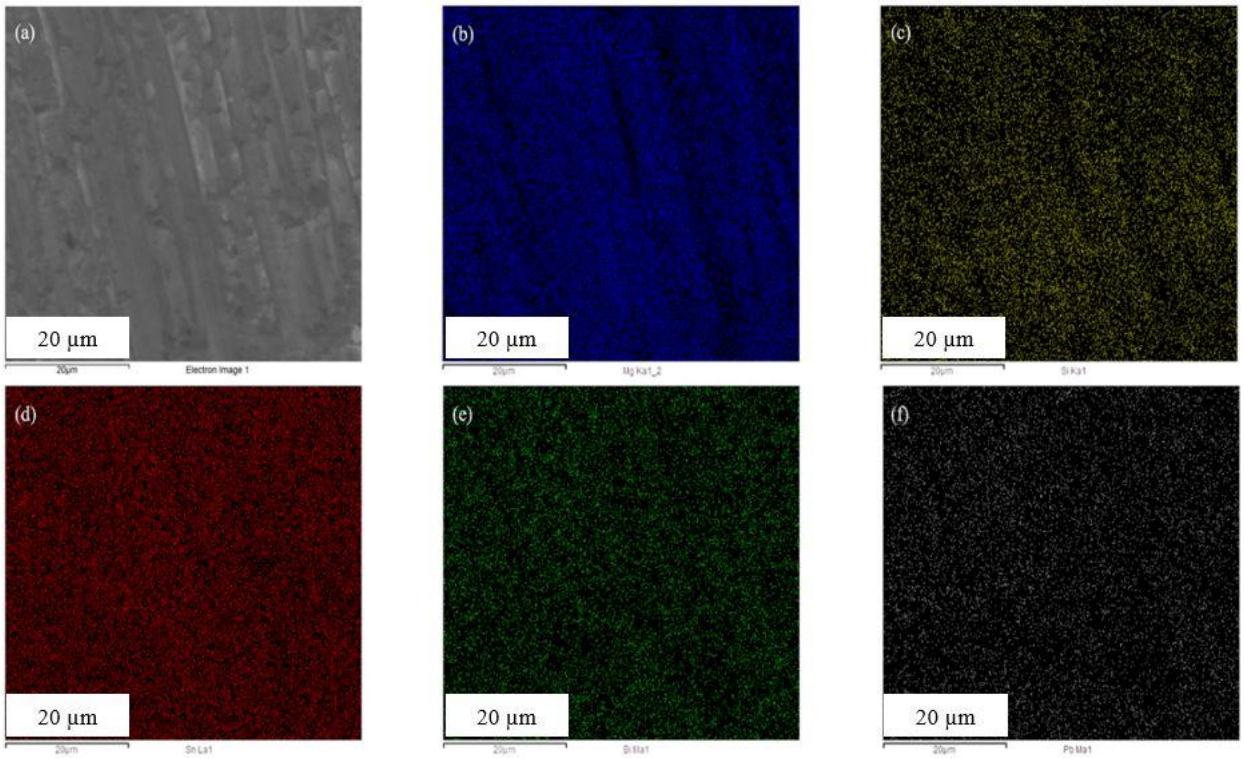


Figure 43. EDX mapping of $Mg_2Si_{0.35}Sn_{0.57}Pb_{0.03}Bi_{0.05}$ sample, with (a) mapping area; (b) Mg; (c) Si; (d) Sn; (e) Bi; (f) Pb represented by different colors.

Table 5. Area scan results (percentages) of $Mg_2Si_{0.35}Sn_{0.55}Pb_{0.05}Bi_{0.05}$ sample.

| Element | Area 1 | Area 2 | Area 3 | Area 4 | Area 5 | Avg. | Nominal |
|---|---|---|---|---|---|---|---|
| Mg | 66.5 | 66.4 | 66.2 | 68.1 | 67.9 | 67.0 | 66.7 |
| Si | 10.7 | 12.7 | 17.5 | 8.3 | 8.4 | 11.5 | 11.7 |
| Sn | 20.2 | 18.2 | 14.8 | 20.6 | 20.6 | 18.9 | 18.3 |
| Bi | 1.5 | 1.6 | 0.9 | 1.5 | 1.7 | 1.4 | 1.7 |
| Pb | 1.2 | 1.2 | 0.6 | 1.5 | 1.4 | 1.2 | 1.7 |

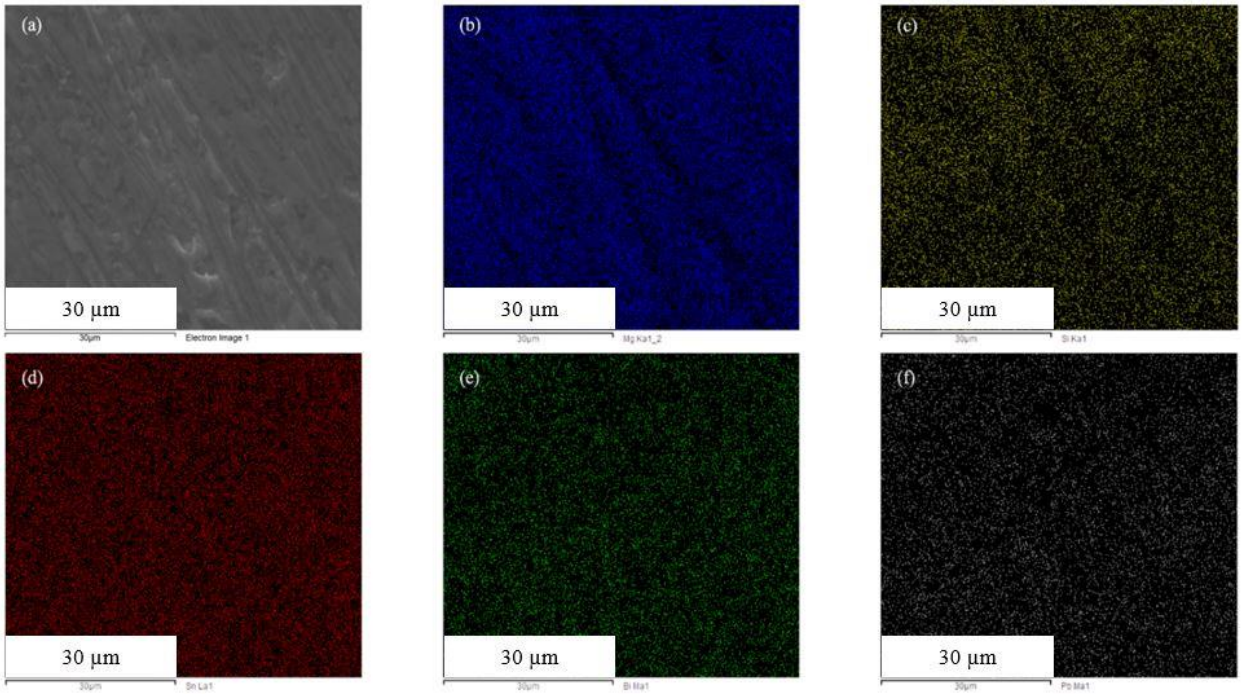


Figure 44. EDX mapping of $Mg_2Si_{0.35}Sn_{0.55}Pb_{0.05}Bi_{0.05}$ sample, with (a) mapping area; (b) Mg; (c) Si; (d) Sn; (e) Bi; (f) Pb represented by different colors.

Table 6. Area scan results (percentages) for $Mg_2Si_{0.35}Sn_{0.53}Pb_{0.07}Bi_{0.05}$ sample.

| Element | Area 1 | Area 2 | Area 3 | Area 4 | Area 5 | Avg. | Nominal |
|---|---|---|---|---|---|---|---|
| Mg | 66.2 | 66.8 | 66.2 | 66.2 | 66.7 | 66.4 | 66.7 |
| Si | 11.2 | 11.7 | 11.8 | 11.8 | 13.2 | 11.9 | 11.7 |
| Sn | 19.1 | 18.2 | 18.5 | 18.4 | 17.1 | 18.3 | 17.6 |
| Bi | 1.4 | 1.4 | 1.5 | 1.7 | 1.6 | 1.5 | 1.7 |
| Pb | 2.1 | 1.8 | 2.1 | 1.9 | 1.4 | 1.9 | 2.3 |

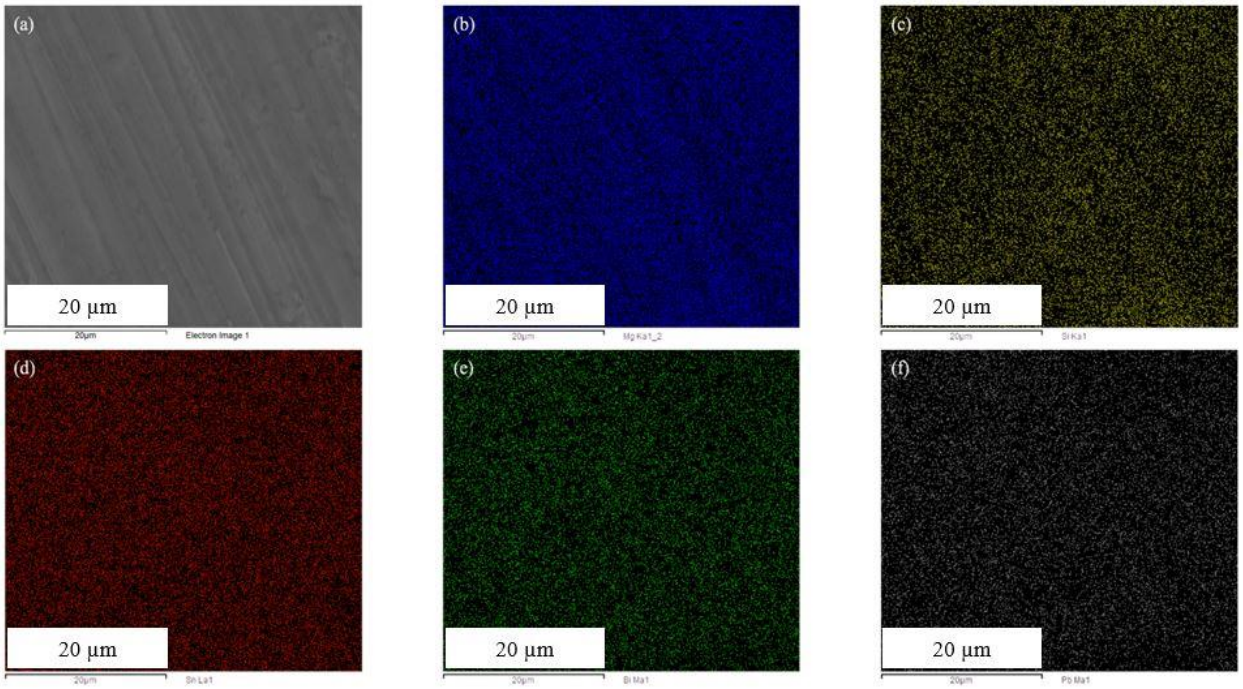


Figure 45. EDX mapping of $Mg_2Si_{0.35}Sn_{0.53}Pb_{0.07}Bi_{0.05}$ sample, with (a) mapping area; (b) Mg; (c) Si; (d) Sn; (e) Bi; (f) Pb represented by different colors.

Table 7. Area scan results (percentages) for $Mg_2Si_{0.35}Sn_{0.5}Pb_{0.1}Bi_{0.05}$ sample.

| Element | Area 1 | Area 2 | Area 3 | Area 4 | Area 5 | Avg. | Nominal |
|---|---|---|---|---|---|---|---|
| Mg | 67.4 | 67.2 | 67.1 | 67.5 | 66.2 | 67.1 | 66.7 |
| Si | 13.4 | 13.8 | 16.3 | 14.6 | 15.1 | 14.6 | 11.7 |
| Sn | 16.0 | 15.5 | 14.2 | 15.2 | 15.7 | 15.3 | 16.7 |
| Bi | 1.2 | 1.2 | 1.0 | 0.9 | 1.0 | 1.1 | 1.7 |
| Pb | 2.0 | 2.3 | 1.4 | 1.8 | 2.0 | 1.9 | 3.3 |

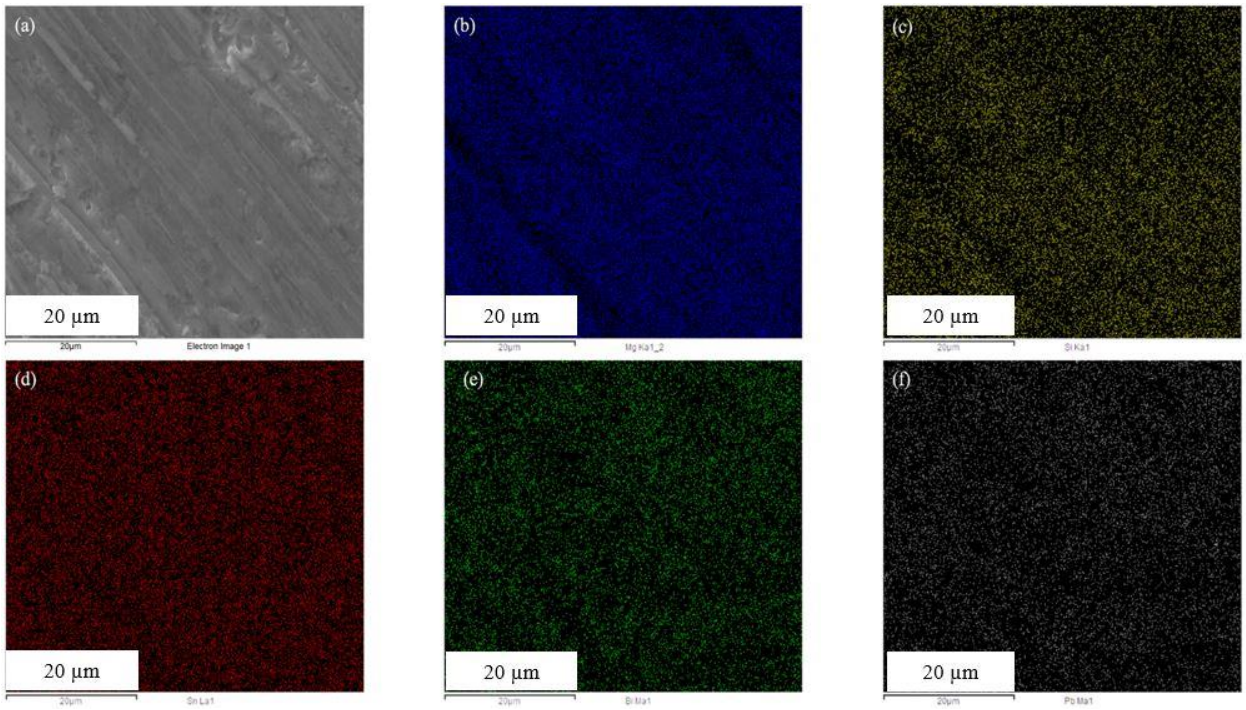


Figure 46. EDX mapping of $Mg_2Si_{0.35}Sn_{0.5}Pb_{0.1}Bi_{0.05}$ sample, with (a) mapping area; (b) Mg; (c) Si; (d) Sn; (e) Bi; (f) Pb represented by different colors.

From Table 3 to Table 7, an increasing amount of Pb, and a decreasing amount of Sn were observed, with Mg, Si, and Bi roughly stayed the same. The trends revealed to be the same as the stoichiometry. The variations between the measured average values and the nominal compositions lie within a reasonable range. The mapping results are demonstrated from Figure 42 to Figure 46, and all the dopants exist in the matrix as solid solutions with even distributions, and there is no aggregation in any particular area.

### 3.5 Physical Property Measurements

The electrical conductivity curves are illustrated in Figure 47. The electrical conductivity for all the samples decreases with rising temperature, proving that all the samples are heavily doped semiconductors. With increasing temperature, the magnitude of the atom vibrations also increases, causing a decrease in the mobility of the charge carriers. This in turn reduces the free mean pass, and as a result, the electrical conductivity is lowered.

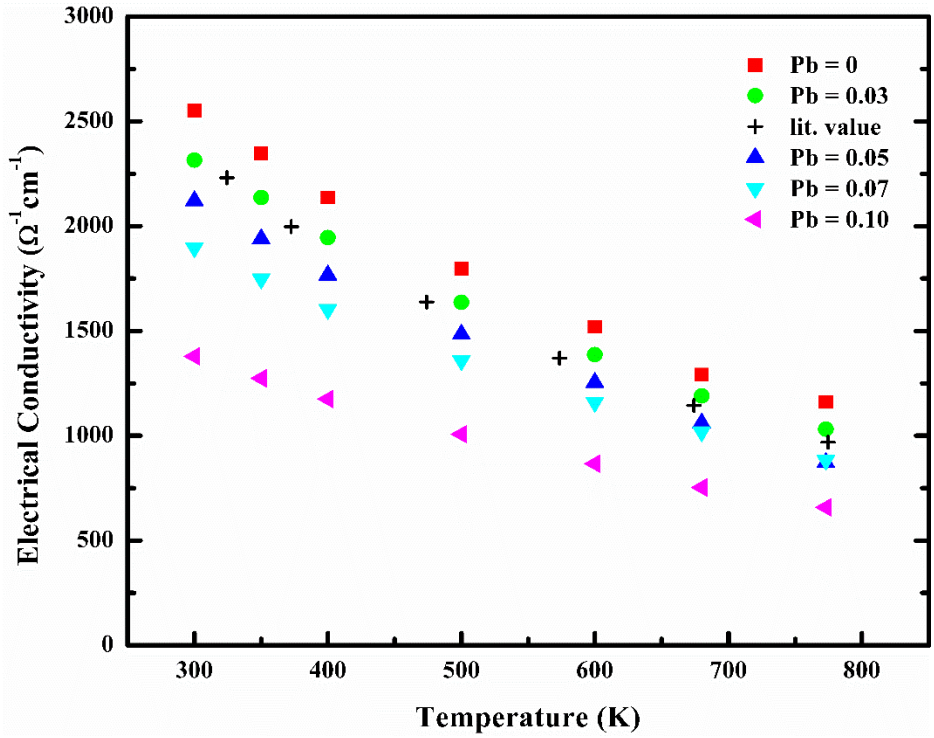


Figure 47. Electrical conductivity of $Mg_2Si_{0.35}Sn_{0.6-x}Pb_xBi_{0.05}$ (x = 0, 0.03, 0.05, 0.07, 0.10), lit. value ($Mg_2Si_{0.365}Sn_{0.6}Bi_{0.05}$) is adopted from [58].

Figure 48 demonstrates the experimental Seebeck coefficient results. All samples revealed negative values as the they are all heavily doped *n*-type semiconductor. The sample with 0 Pb displays a Seebeck coefficient of -105 $\mu VK^{-1}$ at room temperature, and -190 $\mu VK^{-1}$ at 773 K. The sample with 0.05 Pb displays a Seebeck coefficient of -110 $\mu VK^{-1}$ at room temperature, and -200 $\mu VK^{-1}$ at 773 K. There is no significant difference between the results for sample with 0, 0.03, 0.05, 0.07 Pb per formula unit, as the 5% error at this level is around ±5 $\mu VK^{-1}$ at room temperature, and ±10 $\mu VK^{-1}$ at 773 K, the results for these samples remain within the range of the experimental error. However, the sample with 0.10 Pb has a significantly larger Seebeck coefficient compared to the rest samples, with -120 $\mu VK^{-1}$ at room temperature, and -

215 μVK$^{-1}$ at 773 K. In comparison, the sample with similar composition but no Pb ($Mg_2Si_{0.365}Sn_{0.6}Bi_{0.035}$) has a comparable room temperature Seebeck coefficient of around -120 μVK$^{-1}$, and -200 μVK$^{-1}$ at 773 K.[58]

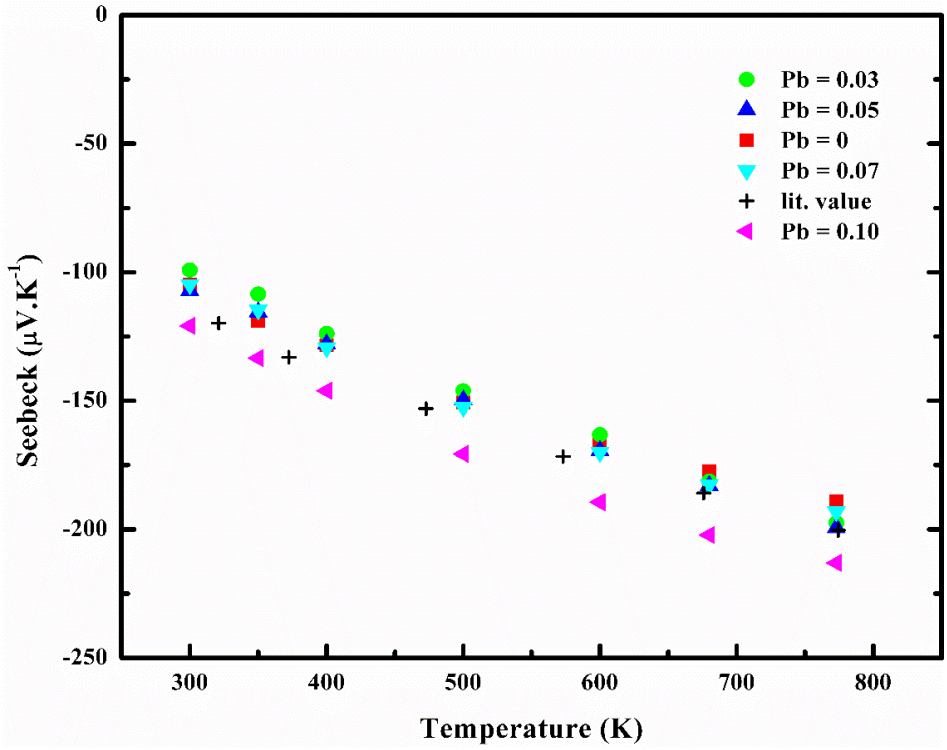


Figure 48. Seebeck coefficient of $Mg_2Si_{0.35}Sn_{0.6-x}Pb_xBi_{0.05}$ (x = 0, 0.03, 0.05, 0.07, 0.10), lit. value ($Mg_2Si_{0.365}Sn_{0.6}Bi_{0.05}$) is adopted from [58].

The enhancement in Seebeck coefficient was reported to be partially related to a band convergence.[103] For the band structures of the $Mg_2(Si,Sn)$ models, one can focus on three bands: one heavy conduction band and one light conduction band on top of the valence band. Depending on the amount of tin, within the composition range from $Mg_2Si_{0.4}Sn_{0.6}$ to $Mg_2Si_{0.35}Sn_{0.65}$, the two conduction bands cross each other. Therefore, the maximum effective

mass was achieved, with equal contributions from both bands, which then increases the Seebeck coefficient. A recent research predicted that a similar band convergence can be achieved with the $Mg_2$(Si, Sn, Pb) system.[151] To validate the assumption, a DFT calculation was performed, and the result for the selected model of $Mg_2Si_{0.4}Sn_{0.6}$, $Mg_2Si_{0.4}Sn_{0.54}Pb_{0.06}$, and $Mg_2Si_{0.4}Sn_{0.51}Pb_{0.09}$ is shown in Figure 49.

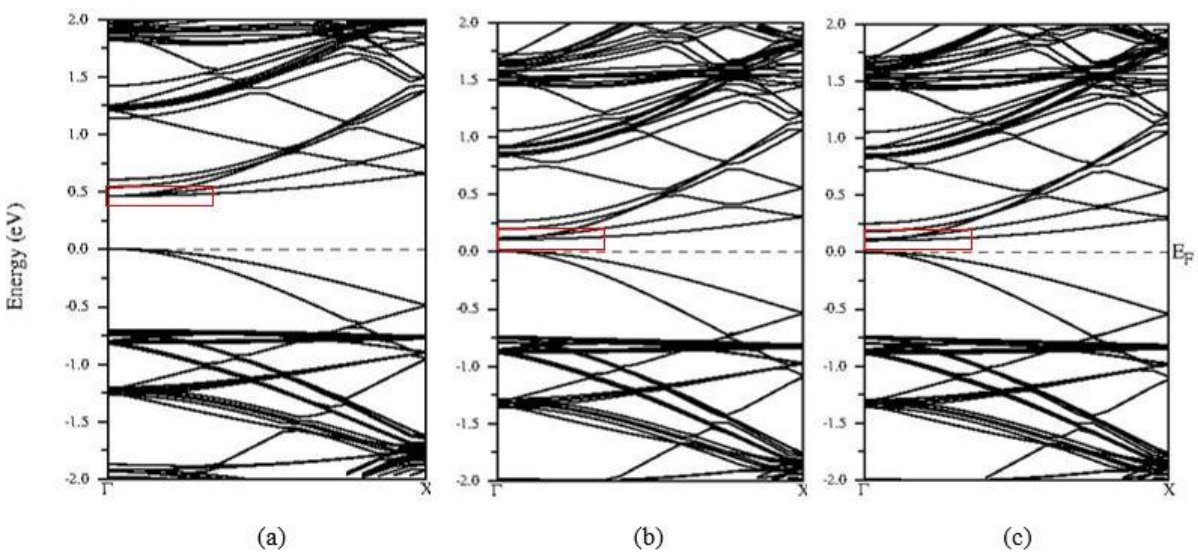


Figure 49. Calculated energy bands ($\Gamma \rightarrow X$), the convergence area is indicated by red line. From left to right: (a) $Mg_2Si_{0.4}Sn_{0.6}$; (b) $Mg_2Si_{0.4}Sn_{0.54}Pb_{0.06}$; (c) $Mg_2Si_{0.4}Sn_{0.51}Pb_{0.09}$.

It is widely known that $Mg_2E$ (E = Si, Ge, Sn) based materials are indirect gap semi-conductors, with the conduction band minimum (CBM) being located at point *X*, and the valence band maximum (VBM) being located at point $\Gamma$. However, in our calculation, both the CBM and VBM are located at point $\Gamma$, which is mainly due to the calculation method that employed a supercell (2 × 2 × 2) to achieve the optimum Si to Sn ratio, and the bands are folded.

To use the appropriate lattice parameters of the electronic structure models, the Vegard's law was employed for calculation. The Vegard's law defines a linear relationship between the composition of a solid solution and its lattice parameter.[152] The reference lattice parameters for the starting compounds were retrieved from literature, and the values are listed in table below.

Table 8. Lattice parameters for electronic structure calculation

| Composition | Lattice Parameter (Å) | Volume (Å$^3$) |
|---|---|---|
| $Mg_2Si$[62] | 6.351 | 256.2 |
| $Mg_2Sn$[64] | 6.765 | 309.6 |
| $Mg_2Pb$[65] | 6.815 | 316.5 |
| $Mg_2Si_{0.4}Sn_{0.6}$ (calc.) | 6.599 | 287.4 |
| $Mg_2Si_{0.4}Sn_{0.54}Pb_{0.06}$ (calc.) | 6.602 | 287.8 |
| $Mg_2Si_{0.4}Sn_{0.51}Pb_{0.09}$ (calc.) | 6.604 | 288.0 |

After the lattice parameters were calculated, a 2 × 2 × 2 supercell was generated using the software named "PowderCell", with a total 32 positions for the E atoms, and 64 positions for Mg atoms. Among the 32 positions for the E atoms, Si atoms occupied 14 positions to achieve a content of approximately 0.4, and the rest 18 positions were mixed occupied by Sn atoms and Pb atoms to achieve the desired composition.

The density field theory was then utilized to calculated the electronic structure for different models using the WIEN2K software package, and the PBE function was employed, which belongs to the generalized gradient approximation (GGA).[142] The structure file generated

was finalized by adding suitable symmetry and the band structure was then calculated. It is worth noting that the density field theory has the known issue of underestimating the band gap. Therefore, the modified Becke-Johnson potential (mBJ) was applied to correct the band gap. The pathway for the calculation was selected only from point $\Gamma$ to $X$, which reduces the duration of the calculation significantly, while sufficient enough to reveal the special band character, as both of the conduction band minimum (CBM) and valence band minimum (VBM) are located within the selected region.

From the calculated result, the assumption is proved that within the studied range, band convergence is retained for the samples with the addition of Pb. Apart from the retained band convergence, the band gap is also significantly reduced with the addition of Pb, with the energy gap for $Mg_2Si_{0.4}Sn_{0.6}$ calculated to be 0.4 eV to 0.5 eV, which is slightly smaller than the literature reported value of 0.6 eV.[61] The energy gap for $Mg_2Si_{0.4}Sn_{0.54}Pb_{0.06}$ is calculated to be around 0.1 eV, and the energy gap for $Mg_2Si_{0.4}Sn_{0.51}Pb_{0.09}$ is calculated to be around 0.1 eV as well.

Figure 50 demonstrates the power factor (*PF*) of all the measured samples, as well as a comparison with the literature values. Below 680 K and 773 K, the *PF* values are comparable for the samples with 0 Pb and 0.03 Pb (both around 40 $\mu Wcm^{-1}K^{-2}$), and also comparable to the highest literature value from the composition of $Mg_2Si_{0.365}Sn_{0.6}Bi_{0.035}$ (40 $\mu Wcm^{-1}K^{-2}$ at 500 K). However, there are no significant differences between the performances of the three samples mentioned above 680 K, as their power factor values all remain within the estimated 7% error (± 3 $\mu Wcm^{-1}K^{-2}$).

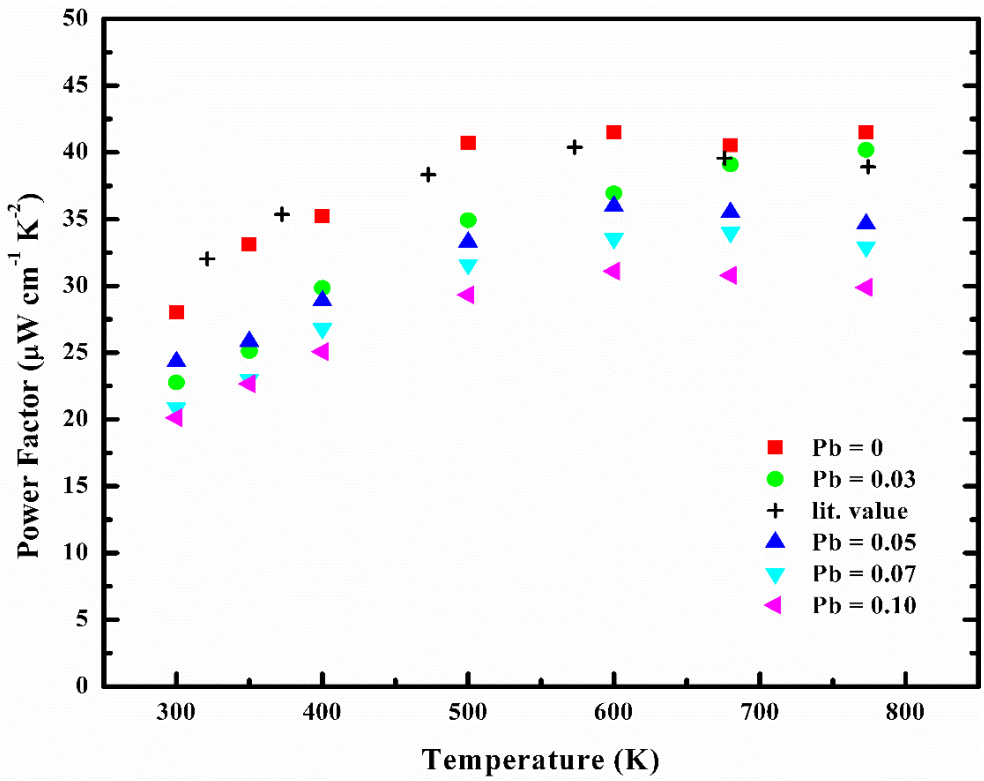


Figure 50. Power Factor (*PF*) of $Mg_2Si_{0.35}Sn_{0.6-x}Pb_xBi_{0.05}$ (x = 0, 0.03, 0.05, 0.07, 0.10), lit. value ($Mg_2Si_{0.365}Sn_{0.6}Bi_{0.05}$) is adopted from [58].

Since the thermal diffusivity measurement machine is temporarily out of order, thermal diffusivity measurements could not be conducted. However, as previously discussed, thermal conductivity consists of two parts: $\kappa_e + \kappa_l$, and $\kappa_e$ can be estimated using Equation 9. The single parabolic band (SPB) model was proved to be as efficient as the three band model calculating the Lorenz number, so the Lorenz number can be determined by using Equation 22.[151]

$$L = \left(\frac{k_B}{e}\right)^2 \left\{\frac{(1+\lambda)(3+\lambda)F_\lambda(\eta)F_{2+\lambda}(\eta) - (2+\lambda)^2 F_{1+\lambda}^2(\eta)}{(1+\lambda)^2 F_\lambda^2(\eta)}\right\} \qquad \text{Equation 22}$$

Where $k_B$ represents Boltzmann constant, $e$ is the charge of electron. With acoustic phonon scattering being the major scattering mechanism, λ can be assumed as zero. $F_\lambda(\eta)$ represents the Fermi-Dirac integral, which can be calculated using Equation 23.

$$S = \frac{k_B}{e}\left\{\frac{(2+\lambda)F_{1+\lambda}(\eta)}{(1+\lambda)F_\lambda(\eta)} - \eta\right\} \qquad \text{Equation 23}$$

Figure 51 demonstrates the calculated Lorenz number for $Mg_2Si_{0.4-x}Sn_{0.6-y}Bi_xPb_y$ (x = 0.05), with the comparison from literature.

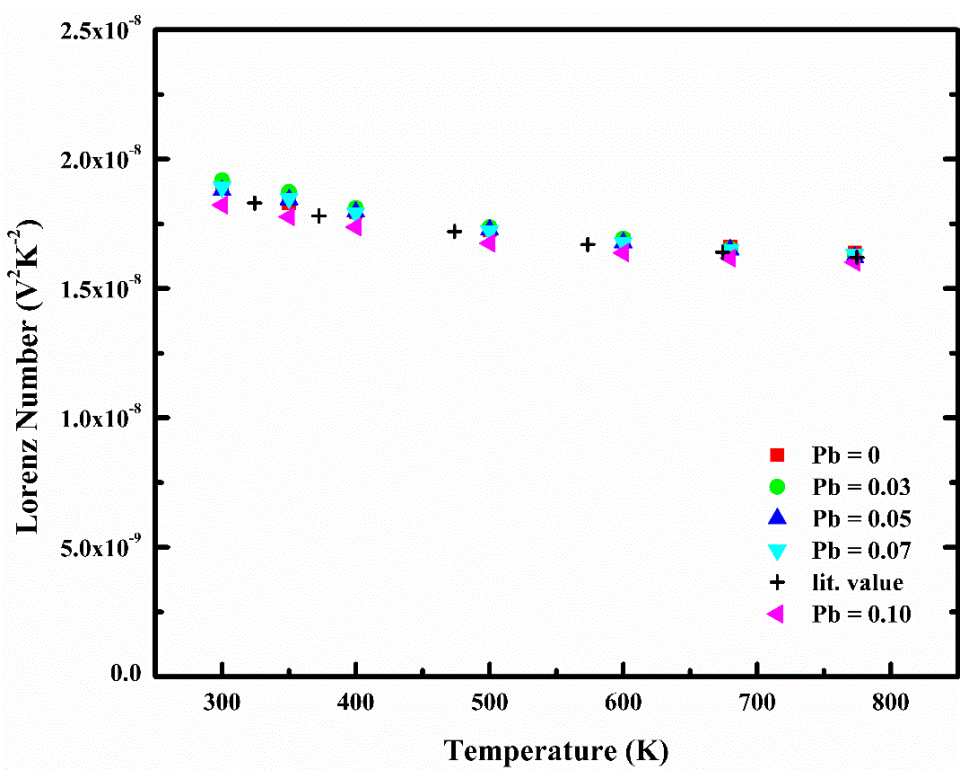


Figure 51. Calculated Lorenz number using SPB model of $Mg_2Si_{0.35}Sn_{0.6-x}Pb_xBi_{0.05}$ (x = 0, 0.03, 0.05, 0.07, 0.10), lit. value ($Mg_2Si_{0.365}Sn_{0.6}Bi_{0.05}$) is adopted from [58].

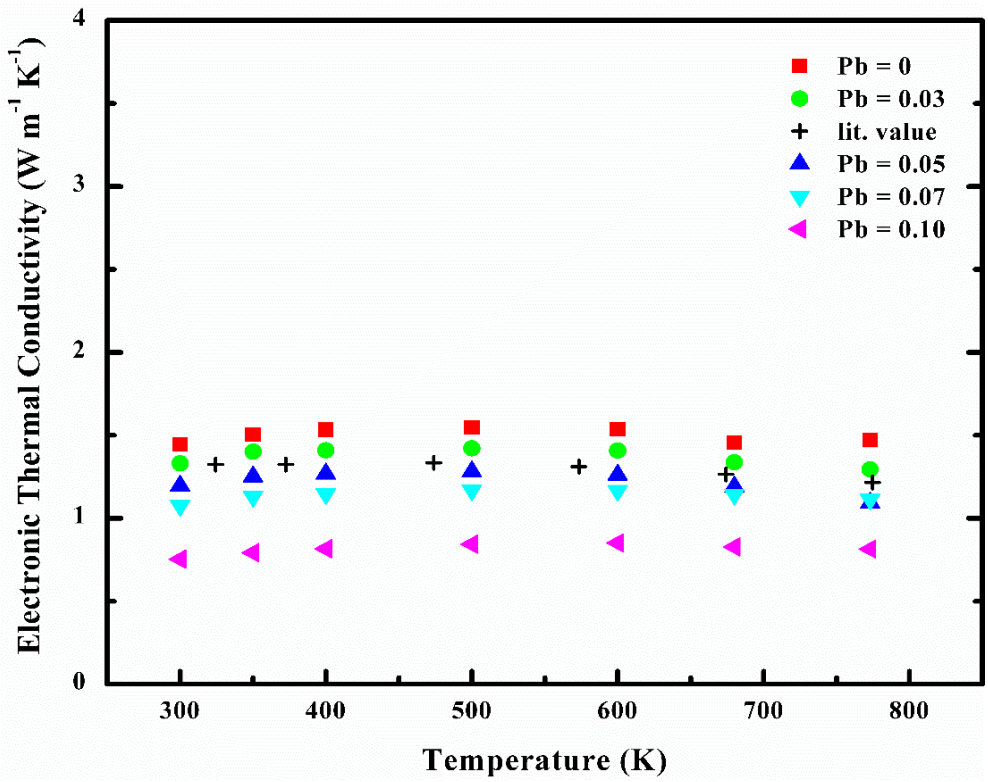


Figure 52. Electronic thermal conductivity of $Mg_2Si_{0.35}Sn_{0.6-x}Pb_xBi_{0.05}$ (x = 0, 0.03, 0.05, 0.07, 0.10), lit. value ($Mg_2Si_{0.365}Sn_{0.6}Bi_{0.05}$) is adopted from [58].

Because of its low electrical conductivity, the sample with 0.1 Pb has the lowest electronic thermal conductivity of 0.75 $W \cdot m^{-1}K^{-1}$ at room temperature, and 0.81 $W \cdot m^{-1}K^{-1}$ at 773 K. The results show a general trend of decreasing electronic thermal conductivity with increasing Pb content. The sample with 0 Pb revealed a consistent electronic thermal conductivity around 1.5 $W \cdot m^{-1}K^{-1}$, which is comparable to a recent literature sample with a composition of $Mg_2Si_{0.365}Sn_{0.6}Bi_{0.035}$ (1.45 $W \cdot m^{-1}K^{-1}$).[58]

The lattice thermal conductivity was then estimated. A standard value was extrapolated from recent literature, with the most similar composition of $Mg_2Si_{0.365}Sn_{0.6}Bi_{0.035}$.[58] The lattice thermal conductivity from literature is illustrated in Figure 53.

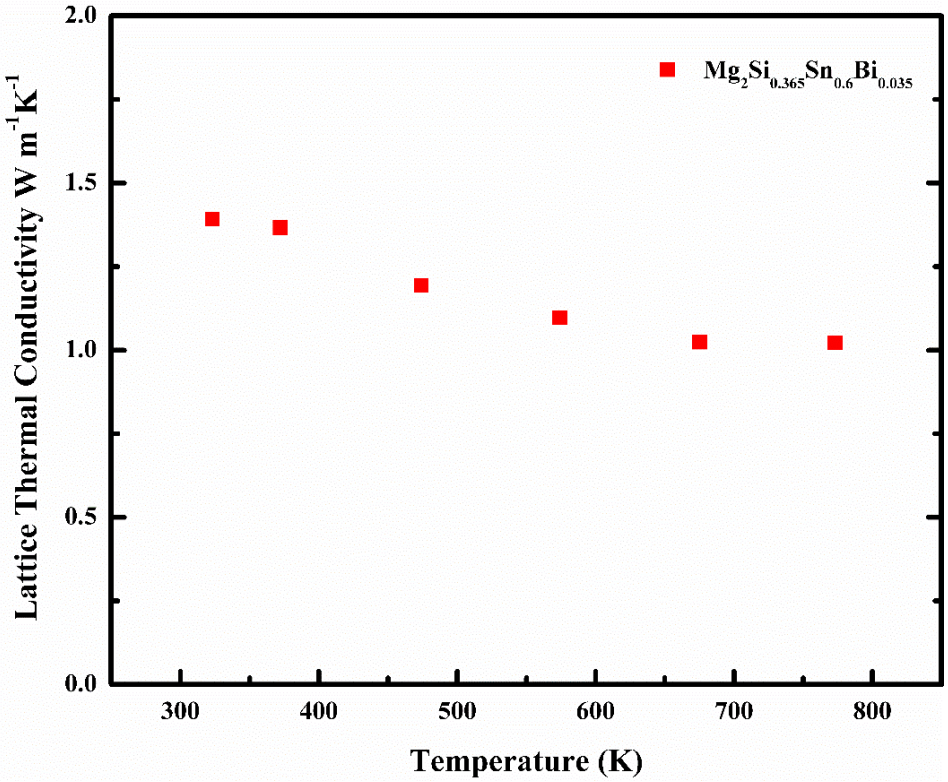


Figure 53. Lattice thermal conductivity of $Mg_2Si_{0.365}Sn_{0.6}Bi_{0.035}$, adopted from [58].

The fitting line was drawn from the experimental data, and the lattice thermal conductivity was drawn from 350 K to 773 K. The total thermal conductivity was then calculated and demonstrated in Figure 54.

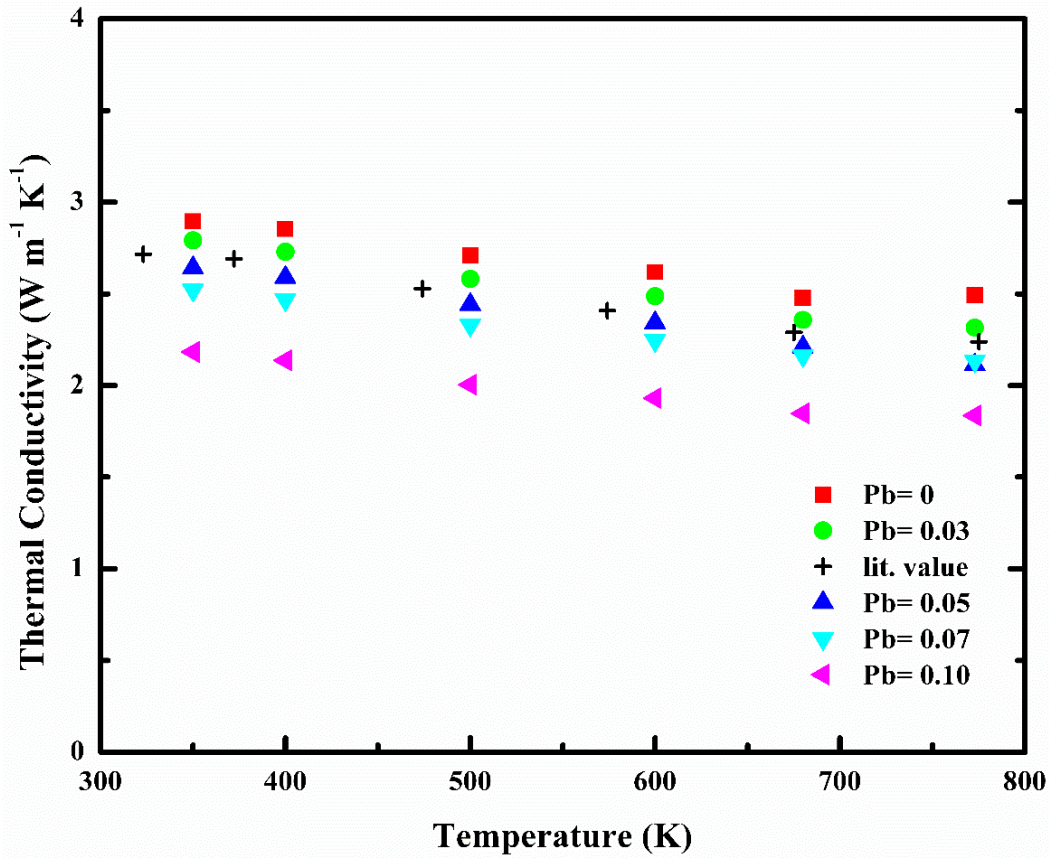


Figure 54. Predicted thermal conductivity of $Mg_2Si_{0.35}Sn_{0.6-x}Pb_xBi_{0.05}$ (x = 0, 0.03, 0.05, 0.07, 0.10), lit. value ($Mg_2Si_{0.365}Sn_{0.6}Bi_{0.05}$) is adopted from [58].

Because the total thermal conductivity is the sum of the lattice thermal conductivity and the electronic thermal conductivity, the total thermal conductivity revealed the same trend as the electrical thermal conductivity, as the lattice thermal conductivity was fixed for a first approximation. The sample with 0 Pb has the highest thermal conductivity of 2.89 $W \cdot m^{-1}K^{-1}$ at 350 K, and reaches its minimum of 2.48 $W \cdot m^{-1}K^{-1}$ at 680 K. The sample with the highest Pb amount has a thermal conductivity of 2.18 $W \cdot m^{-1}K^{-1}$ at 320 K, and reaches the minimum value of 1.84 $W \cdot m^{-1}K^{-1}$ at 773 K.

With the estimated thermal conductivity for all the samples, the estimated figure of merit can then be calculated, and the results are shown in Figure 55.

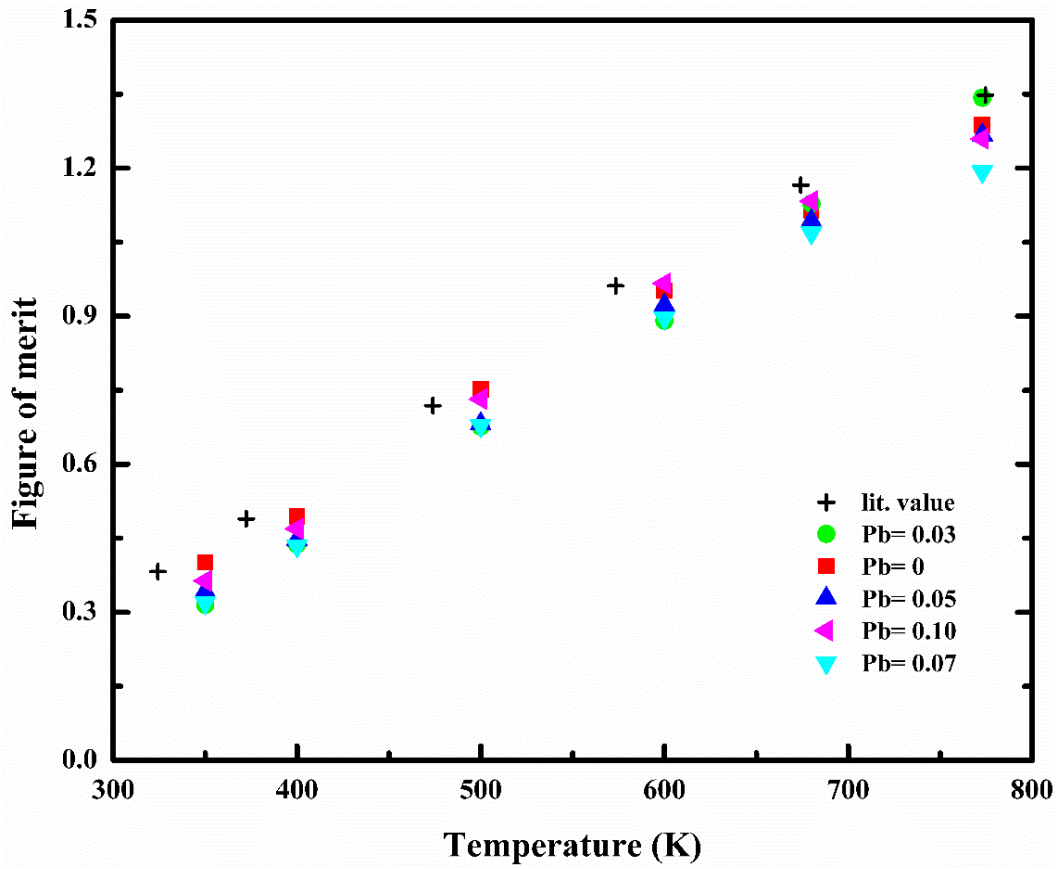


Figure 55. Predicted figure of merit of $Mg_2Si_{0.35}Sn_{0.6-x}Pb_xBi_{0.05}$ (x = 0, 0.03, 0.05, 0.07, 0.10), lit. value ($Mg_2Si_{0.365}Sn_{0.6}Bi_{0.05}$) is adopted from [58].

The figure of merit value increases with increasing temperature for all the samples. The highest value of 1.34 was achieved at 773 K for the sample with 0.03 Pb. At 773 K, the figure of merit values range from 1.2 to 1.3, with an error of ±0.1, despite in part quite different power factor values.

The role of Pb for thermal conductivity was not investigated in this research due to the failure of the instrument. However, recent research reported significantly reduced thermal conductivity values with the addition of different amounts of Pb to $Mg_2Sn_{0.98}Sb_{0.02}$, ranging from 0.05 Pb to 0.25 Pb.[151] The reported reduction in thermal conductivity corresponds well with the assumption being made in this research, but the magnitude of impact from Pb might be different as the reported composition ($Mg_2Sn_{0.98-x}Pb_xSb_{0.02}$) is different compared to the composition employed in this research, which gives different mechanisms for lattice distortions.

Table 9. Physical properties of $Mg_2Si_{0.35}Sn_{0.6-x}Pb_xBi_{0.05}$ (x = 0, 0.03, 0.05, 0.07, 0.10), lit. value ($Mg_2Si_{0.365}Sn_{0.6}Bi_{0.05}$) is adopted from [58].

| Sample | Electrical Conductivity ($\Omega^{-1}cm^{-1}$) | Seebeck Coefficient ($\mu VK^{-1}$) | Power Factor ($\mu Wcm^{-1}K^{-2}$) | Thermal Conductivity ($W \cdot m^{-1}K^{-}$) | Temperature (K) | *ZT* |
|---|---|---|---|---|---|---|
| Pb = 0 | 1160 | -190 | 41 | (2.48) | 773 | (1.29) |
| Pb = 0.03 | 1031 | -200 | 40 | (2.32) | 773 | (1.34) |
| Pb = 0.05 | 870 | -199 | 35 | (2.11) | 773 | (1.27) |
| Pb = 0.07 | 882 | -193 | 33 | (2.13) | 773 | (1.19) |
| Pb = 0.10 | 660 | -215 | 30 | (1.84) | 773 | (1.26) |
| lit. value | 969 | -200 | 40 | 2.24 | 773 | 1.35 |

## 4.0 Conclusion and future work

In this research, the optimization of a systematic synthesis procedure, and the impact of Pb on Bi-doped $Mg_2Si$-$Mg_2Sn$ based thermoelectric material were investigated.

Physical properties were measured and estimated for all the samples in this research. Based on our estimations, samples with compositions of $Mg_2Si_{0.35}Sn_{0.6}Bi_{0.05}$ and $Mg_2Si_{0.35}Sn_{0.57}Pb_{0.03}Bi_{0.05}$ displayed high figure of merit of 1.29 and 1.34, respectively. These results are comparable with some of the best literature values being reported. The estimations made in this research are rather conservative; with the assumption that the thermal conductivity will decrease with the addition of Pb, samples synthesized in this research are most likely going to possess better figure of merit results with valid thermal conductivity measurements. The calculated band structures indicate that the band convergence is retained with the addition of Pb, together with a reduced band gap.

The synthesis method optimized in this research for magnesium silicide stannide based thermoelectric material was proved to be cost-efficient and reproducible. The reduced cost and reduced reaction duration with simplified procedures are beneficial for large scale production, which makes the product more achievable for industrial applications.

For the future work, valid thermal diffusivity measurements are required to prove the assumptions made in this research, as well as calculating more accurate figure of merit values for all the samples. Hall measurements are also important for the evaluation of the carrier concentration, and should therefore be performed in the near future. For theoretical studies, more systematic work is preferred on the band convergence condition for $Mg_2$(Si, Sn, Pb) solid solutions with more Pb content, ideally from 0.05 Pb to 0.5 Pb.

## References


(1) Shafiee, S.; Topal, E. *Energy Policy* **2009**, *37*, 181–189.

(2) Kleinke, H. *Chem. Mater.* **2010**, *22*, 604–611.

(3) Yang, J.; Stabler, F. R. *J. Electron. Mater.* **2009**, *38*, 1245–1251.

(4) Rowe, D. M. *Thermoelectrics Handbook Macro to Nano*, CRC press, New York, USA, **2005**

(5) Tritt, T. M.; Subramanian, M. A. *MRS Bull.* **2011**, *31*, 188–198.

(6) Ioffe, A. F. *Semiconductor Thermoelements, and Thermoelectric Cooling*, Infosearch, London, UK, **1957**.

(7) Szczech, J. R.; Higgins, J. M.; Jin, S. *J. Mater. Chem.* **2011**, *21*, 4037.

(8) Kinzie, P. A. *Thermocouple Temperature Measurement*. Wiley, New York, USA **1973**

(9) Bennett, G.; Lombardo, J.; Hemler, R.; Silverman, G.; Whitmore, C.; Amos, W.; Johnson, E.; Schock, A.; Zocher, R.; Keenan, T.; *et al.*In *4th International Energy Conversion Engineering Conference and Exhibit (IECEC)*; American Institute of Aeronautics and Astronautics: Reston, Virigina, **2006**.

(10) Welch, R.; Limonadi, D.; Manning, R. In *2013 8th International Conference on System of Systems Engineering*; IEEE, **2013**, 70–75.

(11) Simons, R. E.; Chu, R. C. *Sixt. Annu. IEEE Semicond. Therm. Meas. Manag. Symp. (Cat. No.00CH37068)* **2000**, 1–9.

(12) Habman, T. C.; Paris, B.; Miller, S. E.; Goefung, H. L. *J. Phys. Chem. Solids* **1957**, *2*, 181–190

(13) Woollam, J. A.; Beale, H. A.; Spain, I.L. *Properties of Crystalline Bismuth Selenide and Its Use As a Hall Effect Magnetometer.* NASA, Cleveland, USA, **1972**.

(14) Snyder, G. J.; Toberer, E. S. *Nat. Mater.* **2008**, *7*, 105–114.

(15) Hu, L.; Zhu, T.; Liu, X.; Zhao, X. *Adv. Funct. Mater.* **2014**, *24*, 5211–5218.

(16) Xie, W.; Wang, S.; Zhu, S.; He, J.; Tang, X.; Zhang, Q.; Tritt, T. M. *J. Mater. Sci.* **2013**, *48*, 2745–2760.

(17) Faleev, S. V; Léonard, F. *Phys. Rev. B* **2008**, *77*, 214304.

(18) Madavali, B.; Kim, H.S.; Lee, K.H.; Isoda, Y.; Gascoin, F.; Hong, S.J. *Mater. Des.* **2016**, *112*, 485–494.

(19) Li, Y.; Liu, G.; Qin, X.; Shan, F. *RSC Adv.* **2016**, *6*, 112050–112056.

(20) Du, B. L.; Li, H.; Tang, X. F. *J. Alloys Compd.* **2011**, *509*, 2039–2043.

(21) Ye, L. H.; Hoang, K.; Freeman, A. J.; Mahanti, S. D.; He, J.; Tritt, T. M.; Kanatzidis, M. G. *Phys. Rev. B.* **2008**, *77*, 245203.

(22) Hsu, K. F.; Loo, S.; Guo, F.; Chen, W.; Dyck, J. S.; Uher, C.; Hogan, T.; Polychroniadis, E. K.; Kanatzidis, M. G. Science **2004**, *303*, 818–821.

(23) Androulakis, J.; Hsu, K. F.; Pcionek, R.; Kong, H.; Uher, C.; D'Angelo, J. J.; Downey, A.; Hogan, T.; Kanatzidis, M. G. *Adv. Mater.* **2006**, *18*, 1170–1173.

(24) Singh, D. J.; Pickett, W. E. *Phys. Rev. B* **1994**, *50*, 11235–11238.

(25) Caillat, T.; Fleurial, J.; Borshchevsky, A. *J. Cryst. Growth* **1996**, *166*, 722–726.

(26) Jeitschko, W.; Braun, D. *Acta Crystallogr. B Struct. Crystallogr. Cryst. Chem.* **1977**, *33*, 3401–3406.

(27) Chen, B.; Xu, J.; Uher, C.; Morelli, D. T.; Meisner, G. P.; Fleurial, J.-P.; Caillat, T.; Borshchevsky, A. *Phys. Rev. B* **1997**, *55*, 1476–1480.

(28) Nolas, G. S.; Kaeser, M.; Littleton, R. T.; Tritt, T. M. *Appl. Phys. Lett.* **2000**, *77*, 1855–1857.

(29) Shi, X.; Kong, H.; Li, C.-P.; Uher, C.; Yang, J.; Salvador, J. R.; Wang, H.; Chen, L.; Zhang, W. *Appl. Phys. Lett.* **2008**, *92*, 182101.

(30) Guo, Q.; Chan, M.; Kuropatwa, B. A.; Kleinke, H. *Chem. Mater.* **2013**, *25*, 4097–4104.

(31) Guo, Q.; Assoud, A.; Kleinke, H. *Adv. Energy Mater.* **2014**, *4*, 1400348.

(32) Guo, Q.; Kleinke, H. *J. Alloy. Compd.* **2015**, *630*, 37–42.

(33) Vining, C. B.; Fleurial, J. *Proc. Tenth Int. Conf Themoelectrics*, Pasadena, USA, **1993**.

(34) Fano, V. *CRC Handbook of Thermoelectrics*; Rowe, D. M., Ed.; CRC Press, New York, USA, **1995**, 257–266.

(35) LaLonde, A. D.; Pei, Y.; Wang, H.; Snyder, G. J. *Mater. Today* **2011**, *14*, 526–532.

(36) LaLonde, A. D.; Pei, Y.; Snyder, G. J. *Energy Environ. Sci.* **2011**, *4*, 2090–2096.

(37) Pei, Y.; LaLonde, A.; Iwanaga, S.; Snyder, G. J. *Energy Environ. Sci.* **2011**, *4*, 2085–2089.

(38) Wang, H.; Pei, Y.; LaLonde, A. D.; Snyder, G. J. *Adv. Mater.* **2011**, *23*, 1366–1370.

(39) Fu, T.; Yue, X.; Wu, H.; Fu, C.; Zhu, T.; Liu, X.; Hu, L.; Ying, P.; He, J.; Zhao, X. *J. Mater.* **2016**, *2*, 141–149.

(40) Skrabek, E. A.; Trimmer, D. S. *CRC Handbook of Thermoelectrics*; Rowe, D. M., Ed.; CRC Press, New York, USA, **1995**, 267–275.

(41) Davidow, J.; Gelbstein, Y. *J. Electron. Mater.* **2013**, *42*, 1542–1549.

(42) Levin, E. M.; Bud'Ko, S. L.; Schmidt-Rohr, K. *Adv. Funct. Mater.* **2012**, *22*, 2766–2774.

(43) Kim, H.S.; Dharmaiah, P.; Madavali, B.; Ott, R.; Lee, K.H.; Hong, S.J. *Acta Mater.* **2017**, *128*, 43–53.

(44) Ngan, P. H.; van Nong, N.; Hung, L. T.; Balke, B.; Han, L.; Hedegaard, E. M. J.; Linderoth, S.; Pryds, N. *J. Electron. Mater.* **2015**, *45*, 594–601.

(45) Yan, X.; Joshi, G.; Liu, W.; Lan, Y.; Wang, H.; Lee, S.; Simonson, J. W.; Poon, S. J.; Tritt, T. M.; Chen, G.; *et al. Nano Lett.* **2011**, *11*, 556–560.

(46) Wood, D. M.; Zunger, A. *Phys. Rev. B* **1986**, *34*, 4105–4120.

(47) Kurakevych, O. O.; Strobel, T. A.; Kim, D. Y.; Cody, G. D. *Angew. Chemie - Int. Ed.* **2013**, *52*, 8930–8933.

(48) Madelung, O.; Rössler, U.; Schulz, M. *Non-Tetrahedrally Bonded Elements and Binary Compounds I*; Springer-Verlag, Berlin/ Heidelberg, Germany, **1998**.

(49) Nakagawa, R.; Katsumata, H.; Hashimoto, S.; Sakuragi, S.; Morris R. G., R. R. D. and D. G. C.; H., T. J. and K.; H., T. J. and K.; Akasaka M., Iida T., Matsumoto A., Yamanaka K., Takanashi Y., I. T. and H. N.; Ioannou M., Polymeris G. S., Hatzikraniotis E., P. K. M. and K. T.; Sakamoto T., Iida T., Matsumoto A., Honda Y., Nemoto R., Sato J., Nakajima T., T. H. and T. Y.; *et al. Jpn. J. Appl. Phys.* **2015**, *54*, 85503.

(50) Nakagawa, R.; Katsumata, H.; Hashimoto, S.; Sakuragi, S. *Jpn. J. Appl. Phys.* **2015**, *54*, 85503.

(51) Berthebaud, D.; Gascoin, F. *J. Solid State Chem.* **2013**, *202*, 61–64.

(52) Godlewska, E.; Mars, K.; Mania, R.; Zimowski, S. *Intermetallics* **2011**, *19*, 1983–1988.

(53) Yoshinaga, M.; Iida, T.; Noda, M.; Endo, T.; Takanashi, Y. *Thin Solid Films* **2004**, *461*, 86–89.

(54) Itahara, H.; Yamada, T.; Oh, S.Y.; Asahi, R.; Imagawa, H.; Yamane, H. *Chem. Commun.* **2014**, *50*, 4315–4318.

(55) Gao, H.; Zhu, T.; Liu, X.; Chen, L.; Zhao, X. *J. Mater. Chem.* **2011**, *21*, 5933-5937.

(56) Xiong, W.; Qin, X.; Kong, M.; Chen, L. *Trans. Nonferrous Met. Soc. China* **2006**, *16*, 987–991.

(57) Ikeda, T.; Haviez, L.; Li, Y.; Snyder, G. J. *Small* **2012**, *8*, 2350–2355.

(58) Farahi, N.; Prabhudev, S.; Botton, G. A.; Salvador, J. R.; Kleinke, H. *ACS Appl. Mater. Interfaces* **2016**, *8*, 34431–34437.

(59) Buuren, M. R. J. Van; Voermans, F.; Kempen, H. Van. *J. Phys. Chem.* **1995**, *99*, 9519–9522.

(60) Lee, P. M. *Phys. Rev.* **1964**, *135*. A1110-A1114.

(61) Zaitsev, V. K.; Fedorov, M. I.; Gurieva, E. A.; Eremin, I. S.; Konstantinov, P. P.; Samunin, A. Y.; Vedernikov, M. V. *Phys. Rev. B* **2006**, *74*, 045207/1-045207/5.

(62) Noda, Y.; Kon, H.; Furukawa, Y.; Otsuka, N.; Nishida, I. A.; Masumoto, K. *Mater. Trans. JIM* **1992**, *33*, 845–850.

(63) Grosch, G. H.; Range, K.J. *J. Alloys Compd.* **1996**, *235*, 250–255.

(64) Glazov, V. M. *Inorg. Mater* **1965**, *1*, 989.

(65) Fässler, T. F.; Kronseder, C. *New Cryst. Struct.* **1999**, *214*, 438–438.

(66) Jund, P.; Viennois, R.; Colinet, C.; Hug, G.; Fèvre, M.; Tédenac, J. C. *J. Phys. Condens. Matter* **2013**, *25*, 35403.

(67) Kato, A.; Yagi, T.; Fukusako, N. *J. Phys. Condens. Matter* **2009**, *21*, 205801.

(68) Shanks, H. R. *J. Cryst. Growth* **1974**, *23*, 190–194.

(69) Viennois, R.; Jund, P.; Colinet, C.; Tédenac, J. C. *J. Solid State Chem.* **2012**, *193*, 133–136.

(70) Meng, Q. S.; Fan, W. H.; Chen, R. X.; Munir, Z. A. *J. Alloys Compd.* **2011**, *509*, 7922–7926.

(71) Zhou, X.; Wang, G.; Chi, H.; Su, X.; Salvador, J. R.; Liu, W.; Tang, X.; Uher, C. *J. Electron. Mater.* **2012**, *41*, 1589–1594.

(72) Zhang, Q.; Liu, W.; Liu, C.; Yin, K.; Tang, X. F. *J. Electron. Mater.* **2014**, *43*, 2188- 2195.

(73) Sakamoto, T.; Iida, T.; Matsumoto, A.; Honda, Y.; Nemoto, T.; Sato, J.; Nakajima, T.; Taguchi, H.; Takanashi, Y. *J. Electron. Mater.* **2010**, *39*, 1708–1713.

(74) Gao, H.; Zhu, T.; Zhao, X.; Deng, Y. *Dalt. Trans.* **2014**, *43*, 14072–14078.

(75) Kubouchi, M.; Hayashi, K.; Miyazaki, Y. S*cr. Mater.* **2016**, *123*, 59–63.

(76) Itoh, T.; Tominaga, A. *MRS Adv.* **2016**, *1*, 3989–3995.

(77) Hu, X.; Barnett, M. R.; Yamamoto, A. *J. Alloys Compd.* **2015**, *649*, 1060–1065.

(78) Tani, J. I.; Kido, H. *Jpn. J. Appl. Phys.* **2007**, *46*, 3309–3314.

(79) Kaur, K.; Kumar, R. *J. Electron. Mater.* **2017**, *46*, 4682–4689.

(80) Liu, J.-W.; Song, M.; Takeguchi, M.; Tsujii, N.; Isoda, Y. *J. Electron. Mater.* **2016**, *45*, 602–614.

(81) Nieroda, P.; Leszczynski, J.; Kolezynski, A. *J. Phys. Chem. Solids* **2017**, *103*, 147–159.

(82) Kim, G.; Kim, J.; Lee, H.; Cho, S.; Lyo, I.; Noh, S.; Kim, B.W.; Kim, S. W.; Lee, K. H.; Lee, W. *Scr. Mater.* **2016**, *116*, 11–15.

(83) Jung, J. Y.; Kim, I. H. *Electron. Mater. Lett.* **2010**, *6*, 187–191.

(84) Jung, J. Y.; Kim, I. H. *J. Electron. Mater.* **2011**, *40*, 1144–1149.

(85) Kolezynski, A.; Nieroda, P.; Wojciechowski, K. T. *Comput. Mater. Sci.* **2015**, *100*, 84–88.

(86) Tada, S.; Isoda, Y.; Udono, H.; Fujiu, H.; Kumagai, S.; Shinohara, Y. *J. Electron. Mater.* **2013**, *43*, 1580–1584.

(87) Zhang, Q.; Cheng, L.; Liu, W.; Zheng, Y.; Su, X.; Chi, H.; Liu, H.; Yan, Y.; Tang, X.;

Uher, C. *Phys. Chem. Chem. Phys.* **2014**, *16*, 23576–23583.

(88) Saparamadu, U.; de Boor, J.; Mao, J.; Song, S.; Tian, F.; Liu, W.; Zhang, Q.; Ren, Z. *Acta Mater.* **2017**, *141*, 154–162.

(89) Godlewska, E. M.; Mars, K.; Drozdz, P.; Tchorz, A.; Ksiazek, M. *J. Alloys Compd.* **2016**, *657*, 755–764.

(90) Liu, W.; Yin, K.; Su, X.; Li, H.; Yan, Y.; Tang, X.; Uher, C. *Intermetallics* **2013**, *32*, 352–361.

(91) Tang, X.; Zhang, Y.; Zheng, Y.; Peng, K.; Huang, T.; Lu, X.; Wang, G.; Wang, S.; Zhou, X. *Appl. Therm. Eng.* **2017**, *111*, 1396–1400.

(92) Tada, S.; Isoda, Y.; Udono, H.; Fujiu, H.; Kumagai, S.; Shinohara, Y. *Phys. Status Solidi Curr. Top. Solid State Phys.* **2013**, *10*, 1704–1707.

(93) You, S. W.; Shin, D. K.; Kim, I. H. *J. Korean Phys. Soc.* **2014**, *65*, 57–61.

(94) Farahi, N.; Prabhudev, S.; Botton, G. A.; Zhao, J.; Tse, J. S.; Liu, Z.; Salvador, J. R.; Kleinke, H. *J. Alloys Compd.* **2015**, *644*, 249–255.

(95) Zhang, Q.; Zheng, Y.; Su, X.; Yin, K.; Tang, X.; Uher, C. *Scr. Mater.* **2015**, *96*, 1–4.

(96) Tan, X. J.; Liu, G. Q.; Shao, H. Z.; Xu, J. T.; Yu, B.; Jiang, H. C.; Jiang, J. *Appl. Phys. Lett.* **2017**, *110*, 143903.

(97) Muthiah, S.; Pulikkotil, J.; Srivastava, A. K.; Kumar, A.; Pathak, B. D.; Dhar, A.; Budhani, R. C. *Appl. Phys. Lett.* **2013**, *103*, 53901.

(98) Muthiah, S.; Sivaiah, B.; Gahtori, B.; Tyagi, K.; Srivastava, A. K.; Pathak, B. D.; Dhar, A.; Budhani, R. C. *J. Electron. Mater.* **2014**, *43*, 2035–2039.

(99) Tang, X.; Zhang, Y.; Zheng, Y.; Peng, K.; Huang, T.; Lu, X.; Wang, G.; Wang, S.; Zhou, X. *Appl. Therm. Eng.* **2017**, *111*, 1396–1400.

(100) Nikitin, E. N.; Bazanov, V. G.; Tarasov, V. I. *Sov. Phys. Solid State* **1961**, *3*, 2648–2652.

(101) Liu, J.-W.; Song, M.; Takeguchi, M.; Tsujii, N.; Isoda, Y. *J. Electron. Mater.* **2014**, *44*, 407–413.

(102) Zhang, Q.; He, J.; Zhao, X. B.; Zhang, S. N.; Zhu, T. J.; Yin, H.; Tritt, T. M. *J. Phys. D. Appl. Phys.* **2008**, *41*, 185103.

(103) Liu, W.; Tan, X.; Yin, K.; Liu, H.; Tang, X.; Shi, J.; Zhang, Q.; Uher, C. *Phys. Rev. Lett.* **2012**, *108*, 166601.

(104) Shannon, R. D. *Acta Crystallogr. Sect. A* **1976**, *32*, 751–767.

(105) Han, X.; Shao, G. *J. Mater. Chem. C* **2015**, *3*, 530–537.

(106) Kim, S.; Wiendlocha, B.; Jin, H.; Tobola, J.; Heremans, J. P. *J. Appl. Phys.* **2014**, *116*, 153706.

(107) Ihou-Mouko, H.; Mercier, C.; Tobola, J.; Pont, G.; Scherrer, H. *J. Alloys Compd.* **2011**,

*509*, 6503–6508.

(108) Tani, J.; Kido, H. *Intermetallics* **2008**, *16*, 418–423.

(109) Liu, W.; Tang, X.; Sharp, J. *J. Phys. D. Appl. Phys.* **2010**, *43*, 85406.

(110) Liu, W.; Zhang, Q.; Yin, K.; Chi, H.; Zhou, X.; Tang, X.; Uher, C. *J. Solid State Chem.* **2013**, *203*, 333–339.

(111) Zhang, Q.; He, J.; Zhu, T. J.; Zhang, S. N.; Zhao, X. B.; Tritt, T. M. *Appl. Phys. Lett.* **2008**, *93*, 102109.

(112) Liu, W.; Tang, X.; Li, H.; Sharp, J.; Zhou, X.; Uher, C. **2011**, *23*, 5256−5263.

(113) Liu, W.; Tang, X.; Li, H.; Yin, K.; Sharp, J.; Zhou, X.; Uher, C. *J. Mater. Chem.* **2012**, *22*, 13653.

(114) Liu, W.; Zhang, Q.; Tang, X.; Li, H.; Sharp, J. *J. Electr. Mater.* **2011**, *40*, 1062–1066.

(115) Khan, A. U.; Vlachos, N.; Kyratsi, T. *Scr. Mater.* **2013**, *69*, 606–609.

(116) Khan, A. U.; Vlachos, N. V.; Hatzikraniotis, E.; Polymeris, G. S.; Lioutas, C. B.; Stefanaki, E. C.; Paraskevopoulos, K. M.; Giapintzakis, I.; Kyratsi, T. *Acta Mater.* **2014**, *77*, 43–53.

(117) de Boor, J.; Dasgupta, T.; Kolb, H.; Compere, C.; Kelm, K.; Mueller, E. *Acta Mater.* **2014**, *77*, 68–75.

(118) Slifka, J.; Filla, B. J.; Phelps, J. M. *J. Res. Natl. Inst. Stand. Technol.* **1998**, *103*, 357.

(119) Jiang, G.; He, J.; Zhu, T.; Fu, C.; Liu, X.; Hu, L.; Zhao, X. *Adv. Funct. Mater.* **2014**, *24*, 3776–3781.

(120) Gao, P.; Berkun, I.; Schmidt, R. D.; Luzenski, M. F.; Lu, X.; Bordon Sarac, P.; Case, E. D.; Hogan, T. P. *J. Electron. Mater.* **2013**, *43*, 1790–1803.

(121) Du, Z.; Zhu, T.; Chen, Y.; He, J.; Gao, H.; Jiang, G.; Tritt, T. M.; Zhao, X. *J. Mater. Chem.* **2012**, *22*, 6838–6844.

(122) Liu, X.; Zhu, T.; Wang, H.; Hu, L.; Xie, H.; Jiang, G.; Snyder, G. J.; Zhao, X. *Adv. Energy Mater.* **2013**, *3*, 1238–1244.

(123) Ning, H.; Mastrorillo, G. D.; Grasso, S.; Du, B.; Mori, T.; Hu, C.; Xu, Y.; Simpson, K.; Maizza, G.; Reece, M. *J. Mater. Chem. A* **2015**, *3*, 17426–17432.

(124) Migas, D. B.; Bogorodz, V. O.; Filonov, A. B.; Shaposhnikov, V. L.; Borisenko, V. E.; Galkin, N. G. *Jpn. J. Appl. Phys.* **2015**, *54*, 07JA03.

(125) Yang, Z.; Shi, D.; Wen, B.; Melnik, R.; Yao, S.; Li, T. *J. Solid State Chem.* **2010**, *183*, 136–143.

(126) Wen, C.; Nonomura, T.; Kato, A.; Kenichi, Y.; Udono, H.; Isobe, K.; Otake, M.; Kubota, Y.; Nakamura, T.; Hayakawa, Y.; *et al. Phys. Procedia* **2011**, *11*, 106–109.

(127) Imai, Y.; Watanabe, A.; Mukaida, M. *J. Alloys Compd.* **2003**, *358*, 257–263.

(128) Wen, C.; Nonomura, T.; Isobe, K.; Kubota, Y.; Nakamura, T.; Hayakawa, Y.; Kato, A.; Tatsuoka, H. *IOP Conf. Ser. Mater. Sci. Eng.* **2011**, *18*, 142014.

(129) Kuo, Y. K.; Ramachandran, B.; Lue, C. S. *Front. Chem.* **2014**, *2*, 106.

(130) Lue, C. S.; Kuo, C. N.; Huang, J. Y.; Hsieh, H. L.; Liao, H. Y.; Ramachandran, B.; Kuo, Y. K. *J. Phys. D. Appl. Phys.* **2013**, *46*, 315303.

(131) Lue, C. S.; Chou, M. D.; Kaurav, N.; Chung, Y. T.; Kuo, Y. K. *Appl. Phys. Lett.* **2009**, *94*, 192105.

(132) Lue, C. S.; Wong, S. F.; Huang, J. Y.; Hsieh, H. L.; Liao, H. Y.; Ramachandran, B.; Kuo, Y. K. *J. Appl. Phys.* **2013**, *113*, 13710.

(133) West, A. *Solid State Chemistry and Its Applications, 2nd Edition, Student Edition*, John Wiley & Sons, **2014**.

(134) Farahi, N.; Prabhudev, S.; Botton, G. A.; Zhao, J.; Tse, J. S.; Liu, Z.; Salvador, J. R.; Kleinke, H. *J. Alloys Compd.* **2015**, *644*, 249–255.

(135) Suryanarayana, C. *Prog. Mater. Sci.* **2001**, *46*, 1–184.

(136) Bux, S. K.; Fleurial, J. P.; Kaner, R. B.; Vining, C. B.; Matsubara, K.; Seebeck, T. J.; Peltier, J. C.; Wood, C.; Snyder, G. J.; Toberer, E. S.; *et al. Chem. Commun.* **2010**, *46*, 8311–8324.

(137) Riffel, M.; Schilz, J. *XVI ICT "97. Proceedings ICT"97. 16th International Conference on Thermoelectrics (Cat. No.97TH8291)*; IEEE;**1997**, 283–286.

(138) Gao, H.; Zhu, T.; Liu, X.; Chen, L.; Zhao, X. *J. Mater. Chem.* **2011**, *21*, 5933–5937.

(139) Ladd, M.; Palmer, R. *Structure Determination by X-Ray Crystallography*. Springer US, New York, USA, **2013**.

(140) Tritt, T. M. *Thermal Conductivity: Theory, Properties, and Applications*, Kluwer Academic/Plenum Publishers, New York, USA, **2005**.

(141) Gaal, P.; Thermitus, M. A.; Stroe, D. *J. Therm. Anal. Calorim.* **2004**, *78*, 185–189.

(142) Perdew, J. P.; Burke, K.; Ernzerhof, M. *Phys. Rev. Lett.* **1996**, *77*, 3865–3868.

(143) Pulikkotil, J. J.; Singh, D. J.; Auluck, S.; Saravanan, M.; Misra, D. K.; Dhar, A.; Budhani, R. C. *Phys. Rev. B* **2012**, *86*, 1–8.

(144) Kim, G.; Lee, H.; Kim, J.; Roh, J. W.; Lyo, I.; Kim, B. W.; Lee, K. H.; Lee, W. *Scr. Mater.* **2017**, *128*, 53–56.

(145) Jung, I. H.; Kang, D. H.; Park, W. J.; Kim, N. J.; Ahn, S. *Calphad* **2007**, *31*, 192–200.

(146) Nikitin, E. N., Tkalenko, E. N., Zaisev, V. K., Zaslavski, A. I., & Kuznetsov, A. K *J Inorg. Mater* **1970**, *4*, 1656.

(147) Yin, K.; Su, X.; Yan, Y.; You, Y.; Zhang, Q.; Uher, C.; Kanatzidis, M. G.; Tang, X. *Chem. Mater.* **2016**, *28*, 5538–5548.

(148) Liu, W.; Zhang, Q.; Yin, K.; Chi, H.; Zhou, X.; Tang, X.; Uher, C. *J. Solid State Chem.* **2013**, *203*, 333–339.

(149) Zhang, X.; Liu, H.; Lu, Q.; Zhang, J.; Zhang, F. *Appl. Phys. Lett.* **2013**, *103*, 63901.

(150) Price, P. J. CXXXV. *London, Edinburgh, Dublin Philos. Mag. J. Sci.* **1955**, *46*, 1252–1260.

(151) Mao, J.; Wang, Y.; Ge, B.; Jie, Q.; Liu, Z.; Saparamadu, U.; Liu, W.; Ren, Z. *Phys. Chem. Chem. Phys.* **2016**, *18*, 20726–20737.

(152) Denton, A. R.; Ashcroft, N. W. *Phys. Rev. A* **1991**, *43*, 3161–3164.